



ELSEVIER

Finite Elements in Analysis and Design 16 (1994) 99–139

**FINITE ELEMENTS
IN ANALYSIS
AND DESIGN**

Error indicators and adaptive remeshing in large deformation finite element analysis

Nam-Sua Lee, Klaus-Jürgen Bathe*

Department of Mechanical Engineering, Massachusetts Institute of Technology, 77 Massachusetts Avenue, Cambridge, MA 02139, USA

Received June 1993; revised September 1993

Abstract

We present and use a system of adaptive procedures for large-deformation finite element analysis of elastic and elastoplastic problems using the h -refinement approach. The procedures include a pointwise indicator for error in stresses, a pointwise indicator for error in plastic strain increments, a quadrilateral element mesh generator for generating completely new meshes on the deformed configuration of the body, and several mapping schemes for transferring state variables and history-dependent variables accurately across models. These procedures constitute the ingredients of a proposed adaptive scheme that is demonstrated to be effective in solutions of two-dimensional stress analysis problems including contact conditions. An important observation is that with coarse finite element meshes and no error indicator used, crucial physical phenomena may be completely missed in the analysis.

1. Introduction

For more than two decades, the finite element method has been the most effective numerical tool for the analysis of solids and structures [1]. The method however can only provide approximate solutions to a given mathematical model of a physical problem. The magnitude and distribution of the solution errors depend on the finite element discretization used. In nonlinear analysis, the solution errors may also evolve during the incremental solution, making accurate stress predictions very difficult.

Much research effort has been directed towards the development of error estimates, see e.g. [2–6], and adaptive schemes, see e.g. [7–16], so that given an appropriate mathematical model [17], a finite element model can be adaptively refined to achieve any given level of accuracy.

*Corresponding author.

However, the error indicators used in these adaptive schemes are mostly based on integrated quantities (such as strain energies) and the accuracy of pointwise stress results has hardly been directly pursued. Moreover, almost all such research has focused on linear analysis and formidable difficulties still remain in nonlinear analysis where the use of an effective adaptive scheme is even more desirable. In nonlinear analysis, adaptive schemes to simulate metal forming processes have been proposed [18–21], but these schemes largely considered only the use of remodeling techniques to reduce element distortions.

The objective of this work is to formulate and develop a system of numerical procedures for an adaptive scheme that can be effectively used in large-deformation elastic and elastoplastic finite element analysis. We focus our attention on the analysis of two-dimensional plane stress, plane strain and axisymmetric problems using mixed-interpolated quadrilateral finite elements and demonstrate the use of the developed procedures in solutions of some typical large-deformation elastic and elastoplastic problems.

Fig. 1 shows schematically the steps used in solving a nonlinear finite element analysis problem adaptively. In the figure, the “time” (t) simply represents the load or the deformation step in static analysis. The process begins with an initial finite element model that contains an accurate description of the mathematical model considered. The finite element model is solved incrementally using a nonlinear finite element analysis program such as ADINA [22]. At the end of each analysis time step, the solution errors are estimated and element distortions and the adequacy of the contact surfaces are checked. Based on these assessments, it is decided if remeshing is necessary.

Suppose that at time $t + \Delta t$, the solution error at some points in the model has exceeded an acceptable level. The incremental analysis using the current finite element model is then terminated. Based on the distribution of errors at time $t + \Delta t$ and the accuracy level to be achieved by the solution, an effective element-size distribution is derived. A new finite element model is then constructed for time t using a mesh generator so that the required element sizes are achieved everywhere.

Once a new mesh has been created, the solution variables are mapped from the old to the new finite element model and the analysis is continued from time t until the errors again become unacceptably large or element distortions become excessive or additional contact surfaces are needed.

The complete process of analysis proposed in this paper is sought to be carried out in the future interactively by the analyst as the step-by-step solution proceeds.

Considering the contents of the paper, we want to remark upon and introduce the sections as follows.

In general, a reliable analysis should provide accurate displacement and stress predictions. In the displacement-based finite element method, stress predictions are less accurate. The error indicator and refinement procedure should therefore be based on the error in the stresses.

For the solution of problems involving large deformation elastoplastic phenomena, the plastic deformation gradient at time $t + \Delta t$ is obtained from the plastic deformation gradient at time t by a time integration. This procedure leads to errors in the plastic strain increments when the loading is nonradial and the size of the incremental load is too large. It is therefore important to control the incremental load adaptively based on an appropriate error indicator for the plastic strain increments. The formulation of error indicators is discussed in Section 2.

Meshes created by the mesh generator of an adaptive scheme are usually distorted to conform to modeling requirements. Even if an element is initially undistorted, it can become distorted because

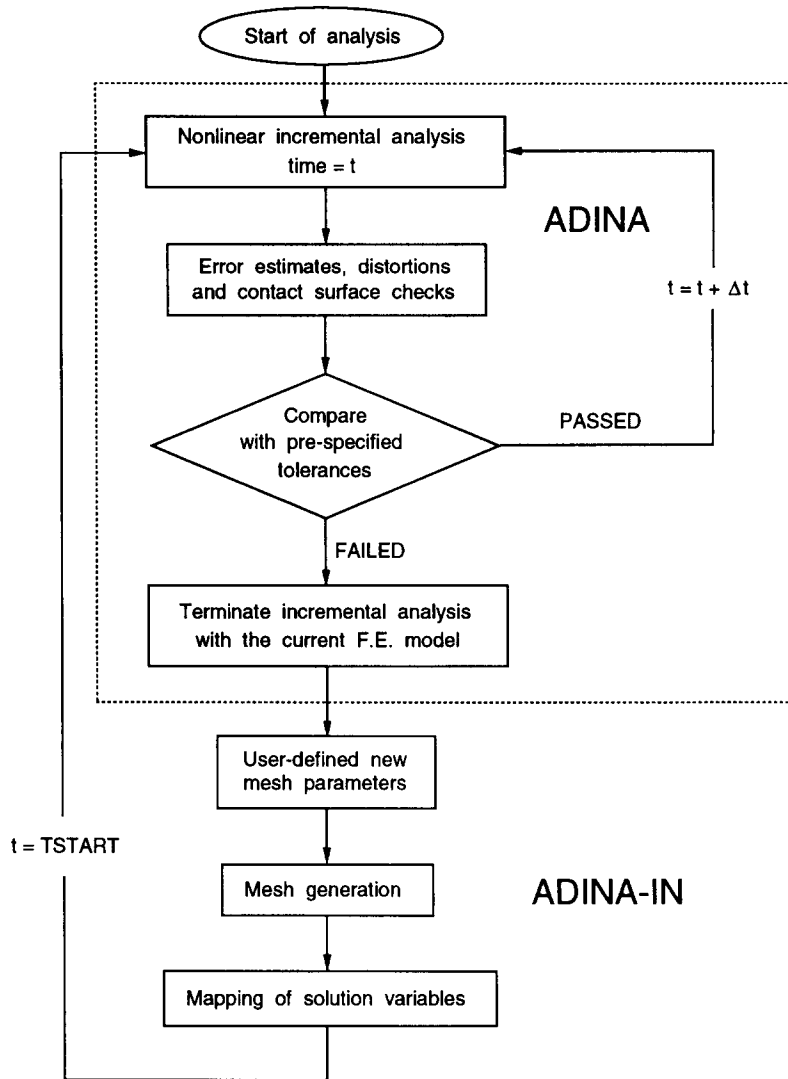


Fig. 1. Outline of adaptive process.

of large deformation effects. It is therefore important to understand the effects of element distortions. For this reason we have completed a systematic study on the effects of element distortions [23] and found that the predictive capabilities of the Lagrangian isoparametric elements are not affected by angular distortions. The serendipity isoparametric elements, on the other hand, are sensitive to such distortions. This finding implies that remeshing schemes can efficiently be based on the use of completely new meshes consisting of Lagrangian elements that may be of trapezoidal or other angular distorted shapes.

Based on the distribution of the error in stresses in the old finite element model and the accuracy level to be achieved by the solution, a new finite element model can be constructed. Three refinement approaches have been proposed and used: the *h*-version [7–9], in which the density of

the finite elements is increased using the same interpolation order in the elements; the p -version [10–12], in which the finite element mesh is fixed and the interpolation order of the elements is increased; and the hp -version [13–16], which is a hybrid of the first two approaches. Our recent study [9] shows the high efficiency of the h -version with Lagrangian elements of order 2, 3 or 4.

For the analysis of highly deformable media such as rubber-like materials (which are nearly incompressible) and elastoplastic materials (which are characterized by plastic deformations that are volume-preserving), it is necessary to use a mixed formulation; notably, the displacement/pressure (or u/p) formulation [24–26]. The 9/3 (9 displacement nodes and 3 pressure variables) mixed-interpolated Lagrangian element, which satisfies the *inf-sup* condition [25], is an effective element for such analysis. We therefore adopt the h -version refinement for our adaptive process and implement our adaptive procedures based on the use of the 9/3 mixed-interpolated Lagrangian element.

For the remeshing, we use a macro-element mesh generator to create an all-quadrilateral element mesh in the deformed configuration. The original geometric boundaries of the old finite element model are preserved by a boundary mapping procedure built into the macro-element mesh generator. These procedures are discussed in Section 3.

Once a new finite element model has been created, the solution variables for the current time step are transferred from the old model to the new model so that the analysis can proceed from the current time step using the new model. In elastic analysis, the solution variables consist of the nodal displacements, the coefficients of the element total pressures (for the u/p formulation), and the variables of the contact algorithm. In elastoplastic analysis, the additional solution variables that have to be transferred are the trial elastic deformation gradient and the equivalent plastic strain, see Section 4.

The developed procedures have been implemented in an experimental manner in subroutines used with the standard object code of the ADINA system, and are demonstrated in the solution of some typical large deformation elastic and elastoplastic problems in Section 5.

2. Error indicators

The error indicators discussed in this section relate to the accuracy of the stresses as measured by the equilibrium error and the plastic strain error.

2.1. Equilibrium error

In the finite element formulation, the equilibrium equations for time t can be derived by applying the principle of virtual work to the body at time t [1]:

$$\int_{tV} {}^t\boldsymbol{\tau} \cdot \delta {}_t\boldsymbol{e} \, dV = \int_{tV} {}^t\boldsymbol{f}^B \cdot \delta \boldsymbol{u} \, dV + \int_{tS_f} {}^t\boldsymbol{f}^S \cdot \delta \boldsymbol{u} \, dS, \quad (1)$$

where δ is the variational operator, ${}_t\boldsymbol{e}$ is the infinitesimal strain tensor, ${}^t\boldsymbol{\tau}$ is the Cauchy stress tensor, ${}^t\boldsymbol{u}$ is the displacement vector with $\delta \boldsymbol{u}$ a variation thereof, ${}^t\boldsymbol{f}^B$ is the prescribed body force vector, ${}^t\boldsymbol{f}^S$ is the prescribed surface traction vector, tV is the volume of the body, and tS_f is the boundary over which tractions are prescribed. Using the same notation as in [1], all quantities with a left

superscript t pertain to the configuration at time t and all quantities with a left subscript t are measured in the configuration at time t . The variations in the displacements must satisfy the condition

$$\delta \mathbf{u} = \mathbf{0} \quad \text{on } {}^tS_u, \tag{2}$$

where tS_u is the boundary over which displacements are prescribed. The admissible displacement variations are \mathcal{H}_0^1 functions:

$$\delta u_i \in \mathcal{H}_0^1. \tag{3}$$

In the finite element formulations, however, Eq. (1) is only satisfied for a subset of the \mathcal{H}_0^1 functions because the actual displacement variations used are

$$\delta \tilde{\mathbf{u}} = \sum_{n=1}^{n_n} \hat{h}_n \delta \hat{\mathbf{u}}_n, \tag{4}$$

where \hat{h}_n are the shape functions associated with node n ($\hat{h}_n \in V_h \subset \mathcal{H}_0^1$); and $\hat{\mathbf{u}}_n$ are the incremental displacements at node n . Also, the body is divided into n_{e1} elements:

$${}^tV = \bigcup_{e=1}^{n_{e1}} {}^tV_e. \tag{5}$$

Denoting the interior inter-element boundaries at time t by ${}^tS_{\text{int}}$

$${}^tS_{\text{int}} = \left(\bigcup_{e=1}^{n_{e1}} {}^tS_e \right) - {}^tS, \tag{6}$$

we can rewrite (1) corresponding to the finite element solution as

$$\sum_{e=1}^{n_{e1}} \int_{{}^tV_e} ((\text{div } {}^t\boldsymbol{\tau}^e + {}^t\mathbf{f}^B) \cdot \delta \tilde{\mathbf{u}} \, dV) - \int_{{}^tS_{\text{int}}} {}^t\mathbf{t}_{\text{jump}} \cdot \delta \tilde{\mathbf{u}} \, dS + \int_{{}^tS_f} ({}^t\mathbf{f}^S - {}^t\mathbf{t}) \cdot \delta \tilde{\mathbf{u}} \, dS = 0, \tag{7}$$

where ${}^t\mathbf{t}$ are the calculated surface tractions on tS_f and ${}^t\mathbf{t}_{\text{jump}}$ are the traction jumps across the inter-element boundaries. Since in the finite element formulation, the equality of Eq. (7) is only enforced for variations $\delta \tilde{\mathbf{u}}_i \in V_h$ and, in general, $V_h \neq \mathcal{H}_0^1$, we have in general:

- the first term of (7) \Rightarrow
within the elements, equilibrium is not satisfied locally; (8)

- the second term of (7) \Rightarrow
across element boundaries, tractions are not equilibrated locally; (9)

- and the third term of (7) \Rightarrow
natural boundary conditions are not satisfied locally. (10)

Based on these observations, various error estimates have been proposed. They include

- body-force-residual type of indicators,
- stress smoothing type of indicators, and
- traction jump type of indicators.

In this paper, we use a pointwise error in stress (EIS) indicator which is a pointwise version of the stress smoothing type of indicators. It can also be thought of as a variation of the Sussman–Bathe stress band plot [3] which has been widely used to indicate the error in stresses (by displaying stress jumps).

The EIS indicator estimates the error in the stresses by giving the differences between the unaveraged stress (τ_{ij}^h) and a smoothed stress (τ_{ij}^*):

$$e_{ij} = |\tau_{ij}^* - \tau_{ij}^h|. \quad (11)$$

The unaveraged stresses are the stresses computed directly by the finite element method. The smoothed stress τ_{ij}^* can be derived from τ_{ij}^h in a variety of ways; for example, using global or local least-squares smoothing [27], local nodal-point averaging [4], or superconvergent patch recovery [6]. We derive our smoothed stresses by projecting the Gauss point stress components bilinearly to the nodal points and then taking the nodal-point averages of these projected values.

In general, only the pressure and the effective stress (which are related to the first and second stress invariants) need to be considered for a complete evaluation of the accuracy of the finite element solution. The smoothed nodal-point pressure (\hat{p}_k^*) and the smoothed nodal-point effective stress ($\hat{\sigma}_k^*$) are calculated from the smoothed stress components at node k . The smoothed pressure (p^*) and the smoothed effective stress (σ^*) within an element are then obtained from \hat{p}_k^* and $\hat{\sigma}_k^*$ by interpolation:

$$p^* = \sum_{k=1}^N h_k(r, s) \hat{p}_k^* \quad (12)$$

and

$$\sigma^* = \sum_{k=1}^N h_k(r, s) \hat{\sigma}_k^*, \quad (13)$$

where the interpolation functions $h_k(r, s)$ are those used for the displacements, k is now the local node number and N is the total number of nodes of the element.

The specific forms of the EIS indicators used in this paper are

$$e_p = \frac{|p^h - p^*|}{(p_{\max}^h - p_{\min}^h)} \times 100\% \quad (14)$$

and

$$e_\sigma = \frac{|\sigma^h - \sigma^*|}{(\sigma_{\max}^h - \sigma_{\min}^h)} \times 100\%, \quad (15)$$

where p_{\max}^h and p_{\min}^h are, respectively, the maximum and minimum values of p^h , and σ_{\max}^h and σ_{\min}^h are, respectively, the maximum and minimum values of σ^h , over the domain where the error is to be evaluated (excluding, for example, regions of singularity where $|p^h|$ and σ^h can be infinitely large). The values of e_p and e_σ thus indicate the pointwise estimated percentage error in pressure and effective stress, respectively.

Once the errors in pressure and effective stress at a particular point have been estimated, we may want to reduce the error at this point by a certain factor, f ; e.g., from 20% to 5% would be a factor

of four. Considering points not near singularities, the rate of convergence of the error in stresses is related to the element size, h , by

$$e_\tau = O(h^p), \quad (16)$$

where p is the order of the interpolation function used. Therefore, to reduce the error by a factor of f , we need to use a new element size

$$h^* = h/f^{1/p}. \quad (17)$$

Once h^* is known over the domain of interest, an optimal mesh can be created with the help of an efficient mesh generator.

2.2. Error in plastic strain increment

In analyses involving elastoplastic response, we use a hyperelastic-based elastoplastic constitutive model formulated using the product decomposition of the deformation gradient and the logarithmic strain measure [28].

Let ${}^0\mathbf{x}$ define the reference configuration at time 0, and let

$${}^t\mathbf{x} = {}^t\mathbf{x}({}^0\mathbf{x}, t) \quad (18)$$

define the current (deformed) configuration at time t . Then, using the notation of [1], the deformation gradient ${}^t_0\mathbf{X}$ at time t is given by

$${}^t_0\mathbf{X} = \frac{\partial {}^t\mathbf{x}}{\partial {}^0\mathbf{x}}. \quad (19)$$

The product decomposition of ${}^t_0\mathbf{X}$ is defined by

$${}^t_0\mathbf{X} = {}^t_0\mathbf{X}^e {}^t_0\mathbf{X}^p, \quad (20)$$

where ${}^t_0\mathbf{X}^e$ and ${}^t_0\mathbf{X}^p$ are, respectively, the elastic and plastic deformation gradients. The plastic deformation gradient corresponds to a deformation from the reference configuration to an intermediate “relaxed” configuration.

Since the plastic deformation is assumed to be incompressible,

$${}^t\mathbf{J}^p = 1, \quad (21)$$

that is

$$\det {}^t_0\mathbf{X}^p = 1. \quad (22)$$

Now, since ${}^tJ = \det {}^t_0\mathbf{X} > 0$, we must have

$${}^tJ^e = \det {}^t_0\mathbf{X}^e = {}^tJ > 0. \quad (23)$$

The elastic deformation gradient therefore admits the polar decomposition

$${}^t_0\mathbf{X}^e = {}^t_0\mathbf{R}^e {}^t_0\mathbf{U}^e, \quad (24)$$

where ${}^t_0\mathbf{R}^e$ is the elastic rotation tensor and ${}^t_0\mathbf{U}^e$ is the right elastic stretch tensor.

We use the Hencky logarithmic strain tensor defined by

$${}^t_0 \boldsymbol{\varepsilon}^e = \ln {}^t_0 \mathbf{U}^e, \quad (25)$$

as the strain measure and its elastic work conjugate, the rotated stress tensor, given by

$${}^t_0 \bar{\boldsymbol{\tau}} = {}^t J ({}^t_0 \mathbf{R}^e)^T {}^t \boldsymbol{\tau} {}^t_0 \mathbf{R}^e, \quad (26)$$

as the stress measure (${}^t \boldsymbol{\tau}$ is the Cauchy stress tensor.)

The stress–strain law is assumed to be

$${}^t_0 \bar{\boldsymbol{\tau}} = \mathcal{L} [{}^t_0 \boldsymbol{\varepsilon}^e], \quad (27)$$

where \mathcal{L} is the fourth-order tensor usually used in small strain history of elastic constants for an isotropic material.

It can be shown that the material symmetry and plastic incompressibility requirements are satisfied if the modified plastic stretching tensor

$${}^t_0 \bar{\mathbf{D}}^p = {}^t_0 \dot{\mathbf{X}}^p ({}^t_0 \mathbf{X}^p)^{-1} \quad (28)$$

is related to the rotated stress tensor by

$${}^t_0 \bar{\mathbf{D}}^p = \chi \dot{\lambda} {}^t_0 \bar{\boldsymbol{\tau}}', \quad (29)$$

where $\dot{\lambda}$ is a proportionality constant yet to be determined; χ is a switching parameter for the rate-independent plasticity such that

$$\chi = \begin{cases} 1 & \text{if } {}^t \sigma = {}^t s \text{ and } {}^t_0 \bar{\boldsymbol{\tau}}' \cdot {}^t_0 \dot{\boldsymbol{\varepsilon}}^e > 0, \\ 0 & \text{if } {}^t \sigma < {}^t s \text{ or } {}^t \sigma = {}^t s \text{ and } {}^t_0 \bar{\boldsymbol{\tau}}' \cdot {}^t_0 \dot{\boldsymbol{\varepsilon}}^e \leq 0, \end{cases} \quad (30)$$

where ${}^t \sigma$ is the effective stress and ${}^t s$ is the yield stress.

The variable $\dot{\lambda}$ in Eq. (29) relates the equivalent plastic strain rate ${}^t \dot{e}^p$ to the effective stress ${}^t \sigma$. This can be seen by setting χ to 1 and taking dot products on both sides of Eq. (29). The result gives

$$\dot{\lambda} = \frac{3}{2} \frac{{}^t \dot{e}^p}{{}^t J {}^t \sigma}, \quad (31)$$

where

$${}^t \dot{e}^p = \sqrt{\frac{2}{3} {}^t_0 \bar{\mathbf{D}}^p \cdot {}^t_0 \bar{\mathbf{D}}^p} \quad (32)$$

and

$${}^t \sigma = \sqrt{\frac{3}{2} {}^t \boldsymbol{\tau}' \cdot {}^t \boldsymbol{\tau}'} = {}^t J^{-1} \sqrt{\frac{3}{2} {}^t_0 \bar{\boldsymbol{\tau}}' \cdot {}^t_0 \bar{\boldsymbol{\tau}}'}. \quad (33)$$

For rate-independent plasticity, the strain hardening function contains the experimental data that relates the yield stress ${}^t s$ to the equivalent plastic strain ${}^t e^p$:

$${}^t s = Y({}^t e^p). \quad (34)$$

The yield surface is defined by

$$\phi({}^t \sigma, {}^t s) = {}^t \sigma - {}^t s = 0. \quad (35)$$

For consistency, we also require that during yielding, the yield stress be equal to the effective stress

$${}^t s = \chi {}^t \sigma. \tag{36}$$

In the numerical implementation, the plastic deformation gradient at time t is obtained from the plastic deformation gradient at time $t - \Delta t$ by integrating the evolution equation for ${}^t_0 X^p$:

$${}^t_0 \dot{X}^p = {}^t_0 \bar{D}^p {}^t_0 X^p \tag{37}$$

over the time interval Δt . This evaluation is achieved using a one-step Euler-backward time-integration procedure:

$${}^t_0 X^p = \exp(\Delta t {}^t_0 \bar{D}^p) {}^{t-\Delta t}_0 X^p, \tag{38}$$

where

$$\Delta t {}^t_0 \bar{D}^p = \Delta e^p = \frac{3}{2} \frac{{}^t e^p - {}^{t-\Delta t} e^p}{{}^t J {}^t \sigma} {}^t_0 \bar{\epsilon}' = \frac{3}{2} \Delta e^p \frac{{}^t_0 \bar{\epsilon}'}{{}^t J {}^t \sigma}. \tag{39}$$

This procedure is computationally stable and yields solutions that satisfy the consistency condition. The accuracy of the solution is also excellent if the loading is radial. However, when the loading is nonradial and a large load step (large Δt) is taken, the procedure may result into significant errors in the plastic strain increment Δe^p and hence significant errors in the plastic deformation gradient ${}^t_0 X^p$.

The exact plastic strain increment is obtained by taking infinitesimally small time-steps from time $t - \Delta t$ to time t :

$$\Delta e^p_{\text{exact}} = \int_{t-\Delta t}^t de^p. \tag{40}$$

At time $t - \Delta t$, de^p is aligned with the direction of ${}^{t-\Delta t}_0 \bar{\epsilon}'$ and at time t , de^p is aligned with the direction of ${}^t_0 \bar{\epsilon}'$. The Euler-backward procedure as given by Eqs. (38) and (39), however, has assumed for the one-step time integration that Δe^p is in the direction of ${}^t_0 \bar{\epsilon}'$ from time $t - \Delta t$ to time t . This assumption leads to errors in Δe^p if ${}^t_0 \bar{\epsilon}'$ is not in the same direction as ${}^{t-\Delta t}_0 \bar{\epsilon}'$ (i.e., if the loading is nonradial). The error in the plastic strain increment tensor is given by

$$\Delta e^p_{\text{error}} = \Delta e^p - \Delta e^p_{\text{exact}}. \tag{41}$$

To obtain an estimate of the error in the plastic strain increment, we calculate the difference between the plastic strain increments obtained using the trapezoidal rule and the Euler-backward method. Hence, we obtain the following indicator for the error in plastic strain increment:

$$\text{EPSI} = \frac{3}{4} \Delta e^p \left\| \frac{{}^t_0 \bar{\epsilon}'}{{}^t J {}^t \sigma} - \frac{{}^{t-\Delta t}_0 \bar{\epsilon}'}{{}^{t-\Delta t} J {}^{t-\Delta t} \sigma} \right\|. \tag{42}$$

For the purpose of implementation, we can rewrite Eq. (42) as

$$\begin{aligned} \text{EPSI} &= \sqrt{\frac{3}{8}} \Delta e^p \left\| \frac{{}^t_0 \bar{\epsilon}'}{\|{}^t_0 \bar{\epsilon}'\|} - \frac{{}^{t-\Delta t}_0 \bar{\epsilon}'}{\|{}^{t-\Delta t}_0 \bar{\epsilon}'\|} \right\| \\ &= \sqrt{\frac{3}{8}} \Delta e^p \left\| \frac{{}^t_0 \epsilon^{e'}}{\|{}^t_0 \epsilon^{e'}\|} - \frac{{}^{t-\Delta t}_0 \epsilon^{e'}}{\|{}^{t-\Delta t}_0 \epsilon^{e'}\|} \right\|, \end{aligned} \tag{43}$$

where ${}^t_0\boldsymbol{\varepsilon}^{e'}$ and ${}^{t-\Delta t}_0\boldsymbol{\varepsilon}^{e'}$ are, respectively, the deviatoric parts of the elastic Hencky strains at time t and $t - \Delta t$. Since these results are already available at each Gauss point, the EPSI indicator can readily be computed using Eq. (43). Alternatively, we may also express the EPSI indicator as a percentage of the total equivalent strain at time t :

$$\% \text{EPSI} = \sqrt{\frac{3}{8}} \frac{\Delta e^p}{{}^t e} \left\| \frac{{}^t_0\boldsymbol{\varepsilon}^{e'}}{\|{}^t_0\boldsymbol{\varepsilon}^{e'}\|} - \frac{{}^{t-\Delta t}_0\boldsymbol{\varepsilon}^{e'}}{\|{}^{t-\Delta t}_0\boldsymbol{\varepsilon}^{e'}\|} \right\| \times 100\%, \quad (44)$$

where the total equivalent strain (${}^t e$) is defined as

$${}^t e = {}^t e^p + {}^t e^e = {}^t e^p + \frac{{}^t \sigma}{E}, \quad (45)$$

with ${}^t e^p$ and ${}^t e^e$, respectively, the equivalent plastic and elastic strains, ${}^t \sigma$ the effective stress, and E the Young's modulus.

3. Mesh generation and remeshing

Suppose that at time $t + \Delta t$, the solution error at some points in the model has exceeded an acceptable level. Based on the distribution of errors and the accuracy level to be achieved by the solution, an effective element-size distribution is derived using the rate of convergence rule. A new model is then constructed for time t so that the required element sizes are achieved everywhere.

It is important that the remeshing be performed on the deformed configuration of the old model (in such a way that the undeformed geometric boundaries of the old model are also preserved). Of course, we could modify the mesh in the undeformed configuration if the mesh is excessively distorted at a certain load step. However, this may lead to large wasted efforts as we cannot predict with certainty whether the improved undeformed mesh will be effective when deformed. A direct and effective way of avoiding excessive element distortions is to mesh the region totally new in the deformed configuration.

3.1. Macro-element mesh generator

For the mesh generation, we use a macro-element mesh generator that creates quadrilateral elements in the deformed configuration. An example of a mesh created by the macro-element mesh generator is shown in Fig. 2. In the figure, A-B-C-D and E-F-G are two examples of macro-elements.

We can characterize an n -sided macro-element by an ordered list of n integer numbers:

$$\mathcal{L} = \{M_1 \ M_2 \ \dots \ M_n\}, \quad (46)$$

where M_i is the element density number at corner i of the macro-element. The element density within each macro-element is assumed to vary uniformly and can therefore be interpolated from the values at the n corners. For examples, $\{4\ 4\ 4\ 4\}$ defines a four-sided macro-element with corner

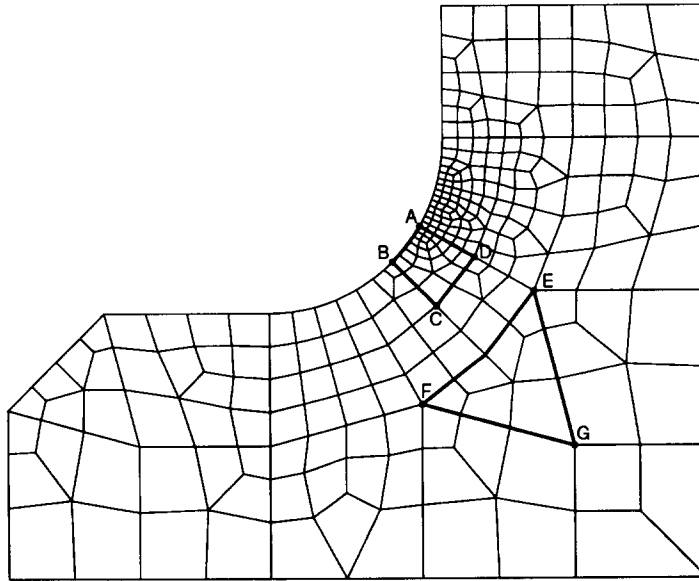


Fig. 2. An example of a mesh constructed using macro-elements.

densities of four elements per side length at all four corners; $\{2248\}$ defines a four-sided macro-element with corner densities of, respectively, 2, 2, 4 and 8 elements per side length; and $\{244\}$ defines a three-sided macro-element with corner densities of, respectively, 2, 4 and 4 elements per side length.

These macro-elements are shown in Fig. 3. The left-hand side of the figure shows the macro-elements in a local r - s plane (a unit-area square) for the four-sided macro-elements or a local r - s - t plane (a unit-area equilateral triangle) for the three-sided macro-element. The right-hand side of the figure shows the actual meshes in the physical domain (i.e., the global x - y plane). The actual meshes are derived from the local meshes by a local-to-global mapping. Since M_i defines the number of elements per side length required at corner i , the order of the entries in \mathcal{L} is important; e.g. $\{2248\}$ and $\{2428\}$ defines two different mesh patterns. However, some of the mesh patterns of the macro-elements are related by rotation or reflection and can be derived from a single mesh pattern plus the appropriate rotation or reflection.

In this paper, we focus our attention on macro-elements characterized by $M_i = 2, 4$ or 8 and $n = 3$ or 4 . Taking into account the similarities, the number of macro-elements characterized by Eq. (46) is only 29 (19 four-sided macro-elements and 10 three-sided macro-elements). These macro-elements are created individually and stored in a library. One other useful macro-element, characterized by $\mathcal{L} = \{1112\}$, is also added to our library. Some of these macro-elements are shown in Figs. 4 and 5.

During the mesh generation, the appropriate macro-element mesh patterns are retrieved from the macro-element library, given the appropriate rotation and reflection and are mapped onto the physical domain to be meshed. For the four-sided macro-elements, we use a bilinearly-blended interpolation formula of Coons [29–31] to map all element-corner nodal points from the local frame to the global frame. The x -coordinate of a nodal-point at the (r, s) location in the local frame

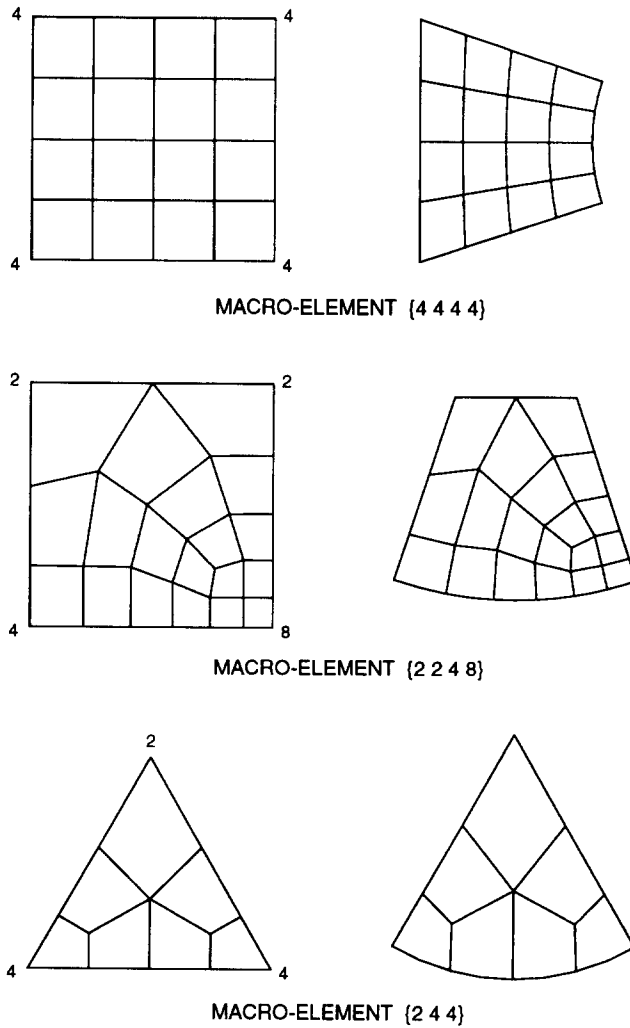


Fig. 3. Examples of macro-elements. On the left, the elements are shown in the local domains, and on the right, the elements are shown in the physical domains.

(see Fig. 6) is obtained from

$$\begin{aligned}
 x(r, s) = & (1 - s)\psi_0(r) + s\psi_1(r) + (1 - r)\xi_0(s) + r\xi_1(s) - (1 - r)(1 - s)x(0, 0) \\
 & - (1 - r)sx(0, 1) - rsx(1, 1) - r(1 - s)x(1, 0), \quad 0 \leq r \leq 1, \quad 0 \leq s \leq 1, \quad (47)
 \end{aligned}$$

where $\psi_0(r), \psi_1(r), \xi_0(s)$ and $\xi_1(s)$ are the x -coordinates of the boundary curves along $s = 0, s = 1, r = 0$ and $r = 1$, respectively. The y -coordinate of the nodal point at (r, s) is similarly obtained.

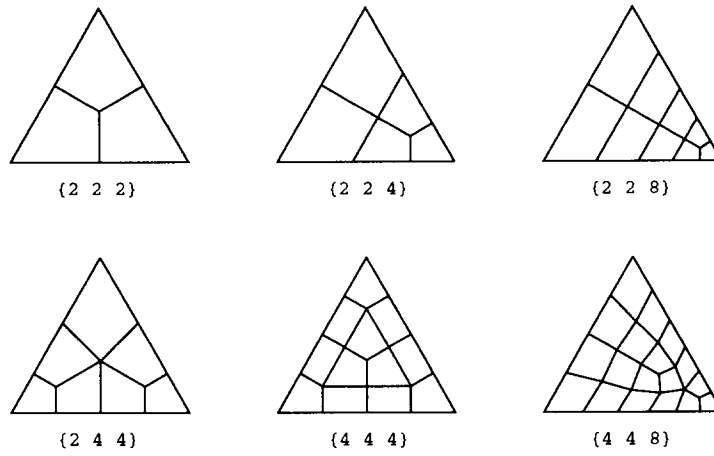


Fig. 4. Some three-sided macro-elements in the library.

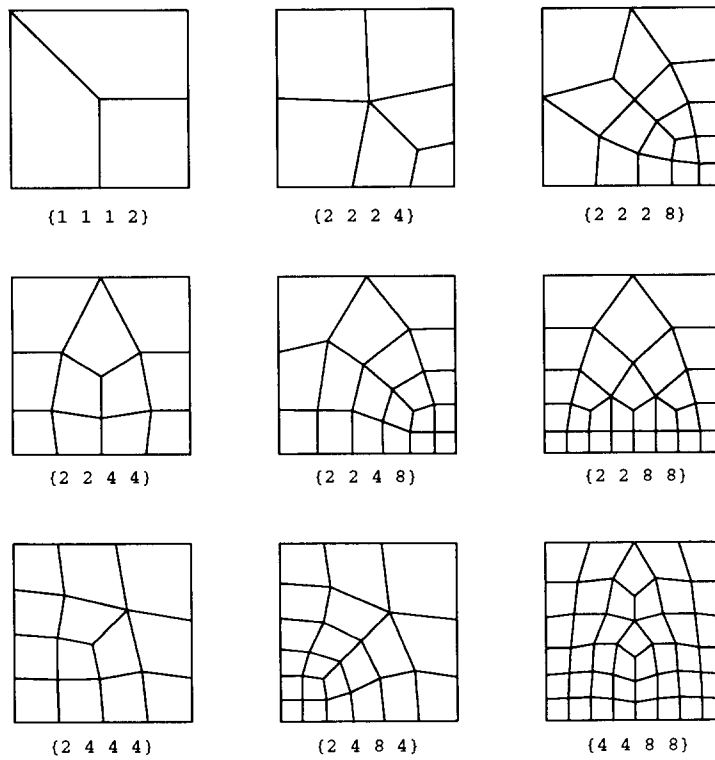


Fig. 5. Some four-sided macro-elements in the library.

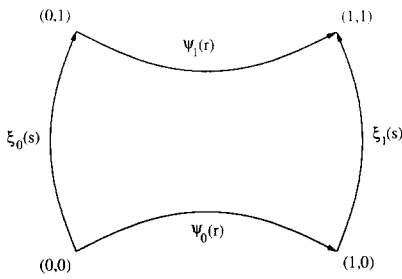


Fig. 6. Bilinear interpolation: coordinate system and boundary curves.

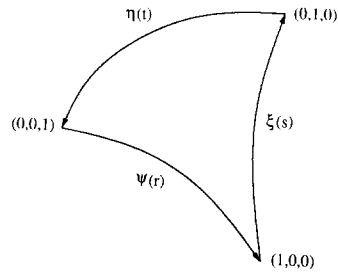


Fig. 7. Trilinear interpolation: coordinate system and boundary curves.

For the mapping of three-sided macro-elements from the local frame to the global frame, we use a trilinearly-blended interpolation formula [31]. The x -coordinate of a nodal-point at the (r, s, t) location in the local frame (see Fig. 7) is obtained from

$$x(r, s, t) = \frac{1}{2} \left[\left(\frac{r}{1-s} \right) \xi(s) + \left(\frac{t}{1-s} \right) \eta(1-s) + \left(\frac{s}{1-t} \right) \eta(t) + \left(\frac{r}{1-t} \right) \psi(1-t) \right. \\ \left. + \left(\frac{t}{1-r} \right) \psi(r) + \left(\frac{s}{1-r} \right) \xi(1-r) - t\psi(0) - r\xi(0) - s\eta(0) \right], \quad (48)$$

where r, s, t are the normalized triangular area coordinates, $0 \leq r \leq 1$, $0 \leq s \leq 1$, $0 \leq t \leq 1$, $r + s + t = 1$; $\psi(r)$, $\xi(s)$ and $\eta(t)$ are the x -coordinates of the boundary curves along $s = 0$, $t = 0$ and $r = 0$, respectively. The y -coordinate of the nodal-point at (r, s, t) is similarly obtained.

The physical coordinates of all nodes that are on the edges and in the interior of all elements, and which do not lie along the boundaries of the domain to be meshed and are not element corner nodes, are interpolated bilinearly from the coordinates of the element corner nodes. This approach ensures that there will be no unevenly-spaced-nodes distortions [23], and curved-edge distortions are present only along the boundaries of the finite element model.

For macro-elements to interconnect properly in a finite element mesh, they must match perfectly along the interface: each side of the interface should have exactly the same number of nodes, location of nodes, number of elements and interpolation order of the elements. These compatibility requirements can be satisfied if all macro-elements are constructed and assembled according to the set of rules given below.

1. The same element interpolation order is used for the entire finite element model.
2. Each edge of the macro-element to be assembled must be connected to a whole number (0, 1, 2, 3 or 4) of edges of macro-elements that have already been assembled.
3. Each edge of the macro-element to be assembled must have exactly the same total number of elements as the combination of all edges to which it is to be connected.
4. If there is a conflict in the placement of nodes along the interfacial edge, the already assembled edges control the actual placement.

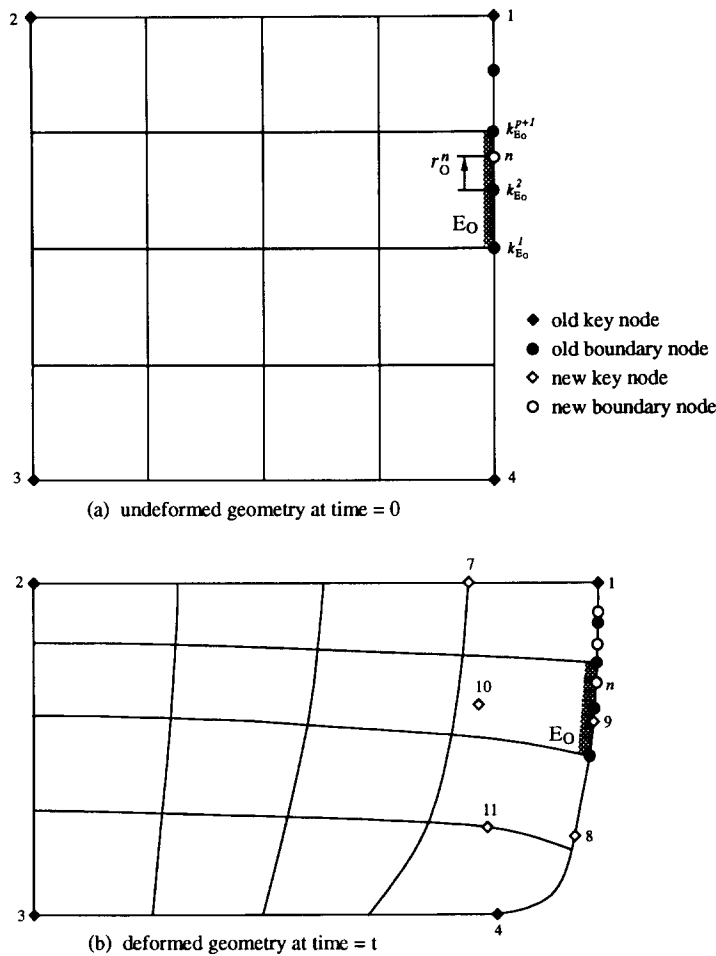


Fig. 8. Mapping of geometric boundary from the old finite element model.

3.2. Remeshing

We perform our remeshing by first dividing the domain, defined by the boundaries of the old model in its deformed configuration, into several three- and four-sided regions. Each of these regions is assumed to be a macro-element. The element-size distribution requirement, dictated by the accuracy criteria, is then translated into a local element density number at each corner of the macro-elements. Macro-elements that have a density number of 9 or more are further divided into smaller macro-elements so that all macro-elements will have corner density numbers of at most 8.

The next step in the remodeling process is to ensure that the edges of the macro-elements along the boundaries of the new finite element model preserve correctly the original geometric boundaries.

Let n be a point that lies on an element edge E_O along a boundary line in the old finite element model; see Fig. 8. We use subscripts O and N to refer to variables and entities belonging to the *old* and the *new* finite element models, respectively. Then the undeformed physical coordinates of

point n are given by

$${}^0\mathbf{x}_O^n = \sum_{k=k_{E_0}^1}^{k_{E_0}^{p+1}} h_k(r_O^n) {}^0\mathbf{x}_O^k, \quad (49)$$

where k is a nodal point on E_O , $k_{E_0}^1$ is the first node and $k_{E_0}^{p+1}$ is the last node on E_O , p being the interpolation order used, h_k is the interpolation function for node k , r_O^n is the local isoparametric coordinate of point n on E_O and ${}^0\mathbf{x}_O^k$ are the undeformed physical coordinates of node k ,

$${}^0\mathbf{x}_O^k = \begin{Bmatrix} {}^0x_O^k \\ {}^0y_O^k \end{Bmatrix}. \quad (50)$$

The deformed boundaries of the body at time t as predicted by the old finite model can also be constructed from the deformed geometry of all element edges that lie along the boundaries. Referring to Fig. 8(b), the deformed physical coordinates of the point n which lies on E_O are given by

$${}^t\mathbf{x}_O^n = \sum_{k=k_{E_0}^1}^{k_{E_0}^{p+1}} h_k(r_O^n) {}^t\mathbf{x}_O^k, \quad (51)$$

where ${}^t\mathbf{x}_O^k$ are the deformed physical coordinates of node k at time t ,

$${}^t\mathbf{x}_O^k = \begin{Bmatrix} {}^tx_O^k \\ {}^ty_O^k \end{Bmatrix}. \quad (52)$$

The objective of the boundary mapping procedure is to transfer accurately the deformed boundary of the old finite element model to the new finite element model in such a way that the original boundary of the body (contained in the old finite element model) is accurately preserved. Preservation of the original boundary is important as we should not be solving a different problem as a result of mapping errors.

To obtain accurately the deformed and undeformed boundaries for the new finite element model, old key nodes on the old finite element model (such as nodes at corners, nodes that define curvatures and indeed all points/nodes that define the geometry of the body) are directly mapped onto the new finite element model; new key nodes along the boundaries (for use as corner nodes of macro-elements) and the remaining boundary nodes of the new finite element model at time t are made to lie on the actual boundary lines of the old finite element model at time t . The undeformed coordinates of point (or node) n could then be obtained from

$${}^0\mathbf{x}_N^n = {}^t\mathbf{x}_N^n - {}^t\mathbf{u}_N^n. \quad (53)$$

Fig. 9 shows the undeformed and deformed geometric boundaries of a new finite element model obtained by applying the boundary mapping procedure to the old finite element model of Fig. 8. Note that the recovered undeformed geometric boundary which consists only of straight edges is exactly the same as in the old model. In general, as long as the geometric boundary of the physical problem consists of piecewise p -order curves (as, for example, provided by a CAD system), any old finite element model consisting of elements of at least order p would have correctly modeled the physical boundary, and any geometric boundary reconstructed for a new finite element model with

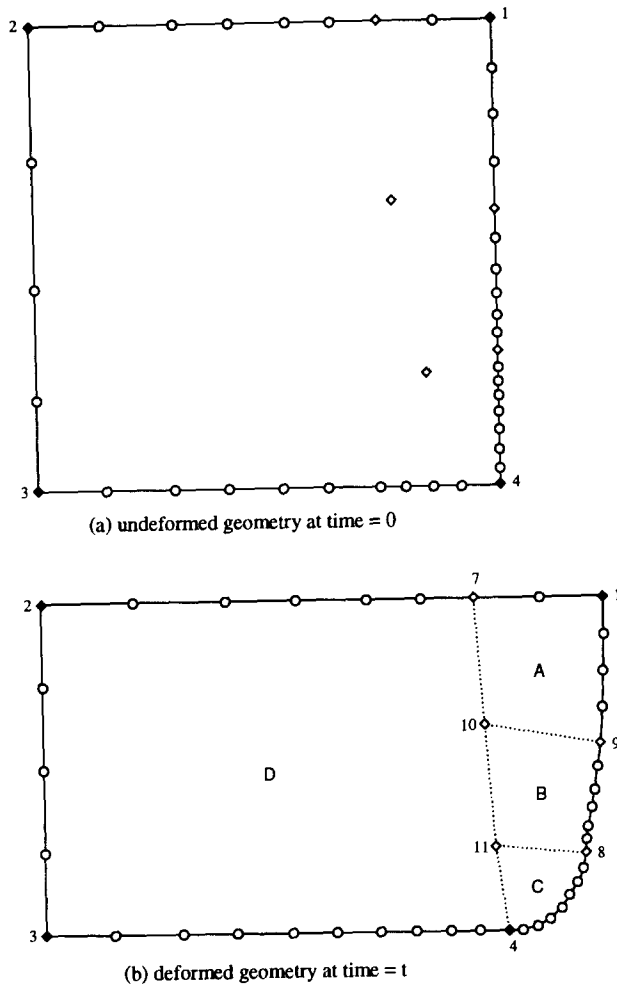


Fig. 9. Mapped geometric boundary for new finite element model.

the above procedure using elements of at least order p would also be able to represent the exact geometric boundary.

Once the edge nodes of the macro-elements along the geometric boundary have been correctly placed, meshing on the deformed configuration can begin. Meshing is performed by mapping the pattern of each macro-element from its local domain to the physical domain. During meshing, a node generator is used to place properly new nodes on the interior macro-element edges. However, if nodes along any of these edges have already been created by another macro-element, the meshing program simply ensures that compatibility requirements (as defined by assembly rules) are satisfied. The sequence of meshing is therefore important. In the example of Fig. 9 the sequence of meshing is A, B, C and then D so that when meshing macro-element D, all edge nodes have already been defined; macro-element D therefore uses the nodes along the interior edges 7-10, 10-11, and 11-4 created when meshing, respectively, macro-elements A, B and C. The resulting mesh pattern for this example created using the above procedure is shown in Fig. 10.

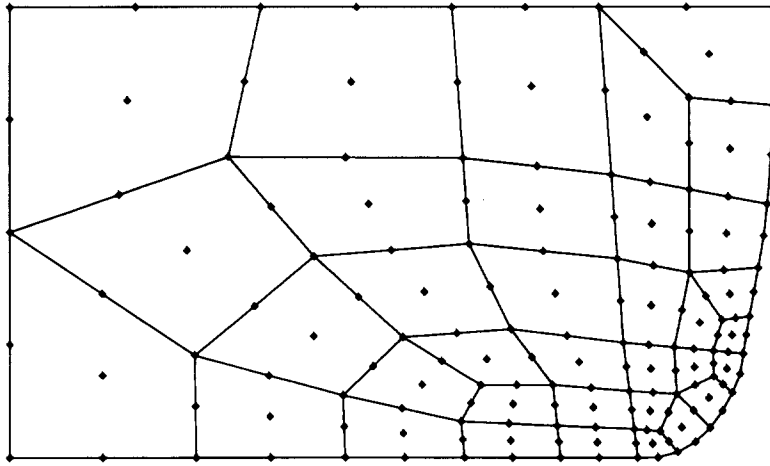


Fig. 10. The new finite element model in the deformed configuration.

4. Mapping of variables

Once a new mesh has been created, state variables and history-dependent variables need to be mapped from the old finite element model to the new model. The state variables consist of the nodal displacements, the coefficients of the element total pressures (for the u/p formulation), and the variables of the contact algorithm. The history-dependent variables consist of the Cauchy stresses, the plastic deformation gradient, the equivalent plastic strain, the yield stress and the elastoplastic flag.

Let ${}^t\mathbf{u}_O$ be the displacement field given by the old finite element model at time t , and ${}^t\mathbf{u}_N$ be the displacement field given by the new finite element model at time t . Note that both finite element models occupy the same domain tV at time t . The displacement mapping process can be stated as

$${}^t\mathbf{u}_O({}^tV) \rightarrow {}^t\mathbf{u}_N({}^tV). \quad (54)$$

Fig. 11 illustrates the displacement mapping, with n denoting a nodal point of the new finite element model where the unknown displacement ${}^t\mathbf{u}_N^n$ is sought, and k ($k = 1, \dots, K_O$) denoting the local nodes of element E_O in the old finite element model containing node n .

The mapping process for the other variables can be stated in a similar manner as

$${}^t\mathbf{p}_O({}^tV) \rightarrow {}^t\mathbf{p}_N({}^tV) \quad (55)$$

and

$${}^t\mathbf{l}_O({}^tV) \rightarrow {}^t\mathbf{l}_N({}^tV), \quad (56)$$

where ${}^t\mathbf{p}_O, {}^t\mathbf{l}_O$ and ${}^t\mathbf{p}_N, {}^t\mathbf{l}_N$ are, respectively, the element pressure coefficients and the list of history-dependent variables of the old and new finite element models. Note that node n would actually be a Gauss (integration) point when mapping pressure- and history-dependent variables.

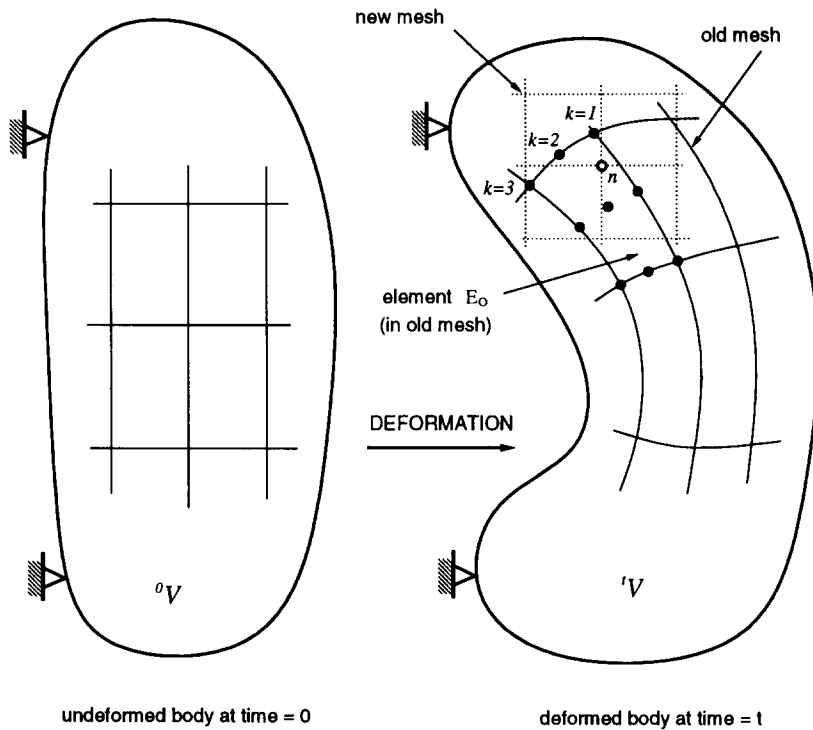


Fig. 11. Deformed geometry displacement mapping.

The mapping processes consist of essentially three steps:

1. Element identification (EI) – to identify the element E_0 that contains node n .
2. Isoparametric inversion (IM^{-1}) – to determine the (r_0^n, s_0^n) coordinates of node n in element E_0 .
3. Data transfer – to transfer data (values of variables) at the (r_0^n, s_0^n) location in element E_0 to node n .

The element identification (EI) and isoparametric inversion (IM^{-1}) procedures are the same for all the mapping processes and are presented in the next section where we also discuss the procedure for displacement mapping. The procedures for mapping of pressure, contact conditions and history-dependent variables are presented thereafter.

4.1. Mapping of displacements

Before the solution variables can be transferred from E_0 of the old finite element model to node n of the new finite element model, we must first determine which is the element E_0 that contains node n . Since this task has to be performed for every nodal and Gauss (integration) point in the new finite element model, it is important that a reliable and computationally efficient procedure be used. We employ an identification procedure that uses a “polygon bounding box” to determine if a node is in E_0 .

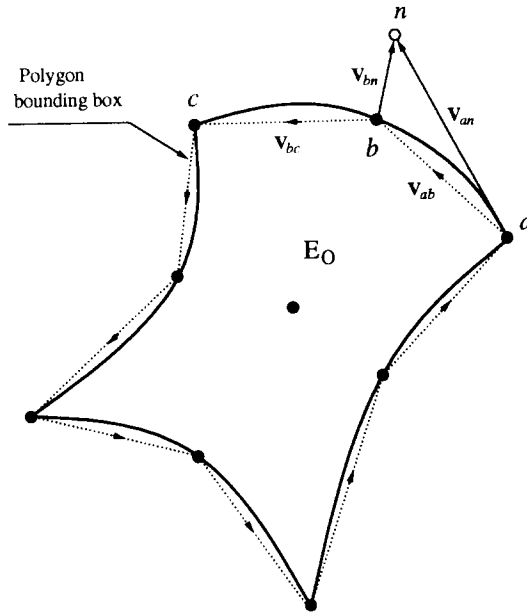


Fig. 12. Element identification using a polygon bounding box.

The polygon bounding box for a 9-node element E_O is shown in Fig. 12. Each side of the polygon is formed by two adjacent nodes of element E_O . Conceptually, to determine if node n is inside element E_O , we move in an anticlockwise direction along the edges of the polygon; node n is deemed to be inside element E_O if the node is always on our left during the travel; otherwise, subject to the following further use of a tolerance, the node is deemed to be outside element E_O . Namely, for element edges that are convex outwards, a nearness tolerance is used to ensure that all nodes between the polygon edges (e.g., the straight edge $a-b$ in Fig. 12) and the element edges (curved edge $a-b$ in Fig. 12) are correctly identified as being inside the element. It is most important that the identification procedure correctly identifies a node as inside E_O if the node is actually inside E_O because any node that is “lost” (not being identified as inside E_O when it should have been) cannot participate during data transfer. At a lost node, data transfer procedures simply do not know where to transfer the solution from.

The nodes $a-b-c$, as shown in Fig. 12, are three nodes on an edge of a 9-node element E_O . Let

$$\alpha_{anb} = V_{an} \times V_{ab}, \tag{57}$$

$$\alpha_{bnc} = V_{bn} \times V_{bc}, \tag{58}$$

and

$$\beta_{abc} = V_{ab} \times V_{bc}. \tag{59}$$

For the case of element edge $a-b-c$ being convex outwards, we can show that if node n lies inside or on the curved element edge $a-b-c$, $\alpha_{anb} \leq \frac{1}{8} \beta_{abc}$ and $\alpha_{bnc} \leq \frac{1}{8} \beta_{abc}$. We therefore consider node n to

be inside E_O if

$$\alpha_{anb} \leq \frac{1}{8} \max(\beta_{abc}, 0) \text{ and } \alpha_{bnc} \leq \frac{1}{8} \max(\beta_{abc}, 0) \tag{60}$$

for all four sides of element E_O .

Once we have identified the element E_O in the old model that contains node n (n may also be a Gauss point) of the new model, we next have to obtain the isoparametric coordinates (r_O^n, s_O^n) of node n in element E_O . Let h_k be the interpolation function corresponding to node k ; then

$${}^t\mathbf{x}_N^n = \sum_{k=1}^{K_O} h_k(r_O^n, s_O^n) {}^t\mathbf{x}_O^k, \tag{61}$$

where

$${}^t\mathbf{x}_N^n = \begin{Bmatrix} {}^t x_N^n \\ {}^t y_N^n \end{Bmatrix} \tag{62}$$

are the physical coordinates of node n and

$${}^t\mathbf{x}_O^k = \begin{Bmatrix} {}^t x_O^k \\ {}^t y_O^k \end{Bmatrix} \tag{63}$$

are the physical coordinates of node k ($k = 1, \dots, K_O$). Since the physical coordinates of all nodes and Gauss points in both the old and new finite element models are known, we may use Eq. (61) directly to solve for (r_O^n, s_O^n) . If $-1 \leq r_O^n \leq +1$ and $-1 \leq s_O^n \leq +1$ then node n is actually in E_O ; otherwise, the element identification procedure is repeated to search for another element that may contain node n (which can happen when node n is beside a curved edge).

Several numerical methods have been proposed to obtain the solution of Eq. (61) [32, 33]; however, none of these methods is effective enough to deal with elements of any order. Although in this paper, we focus our attention on an h -adaptive scheme using the 9-node Lagrangian element, we would like our adaptive procedures to be general enough to be applicable to elements of any order with little or no change in the formulation, so that we can easily extend the developed scheme to also use lower- or higher-order Lagrangian elements. We therefore use a direct Newton–Raphson iteration scheme to solve Eq. (61), which can be employed for elements of any order. The method is also very accurate and converges at a quadratic rate. We shall refer to this method of obtaining the isoparametric coordinates (r_O^n, s_O^n) of node n in element E_O as the *inverse isoparametric mapping technique*.

Once r_O^n and s_O^n have been found, the displacement at node n , ${}^t\mathbf{u}_N^n$ is obtained directly from

$${}^t\mathbf{u}_N^n = \sum_{k=1}^{K_O} h_k(r_O^n, s_O^n) {}^t\mathbf{u}_O^k. \tag{64}$$

4.2. Mapping of pressure variables

In the u/p formulation, the pressure ${}^t\tilde{p}_O$ of the old finite element model is interpolated elementwise and separately from the displacement field [24]. Namely,

$${}^t\tilde{p}_O(r_O, s_O) = \sum_{m=1}^{M_O} g_m(r_O, s_O) {}^t p_O^m, \tag{65}$$

where the ${}^t p_O^m$ are pressure coefficients (element internal variables), the $g_m(r_O, s_O)$ are pressure interpolation functions and M_O is the number of terms used in the pressure interpolation (all quantities pertaining to the old finite element model). Since the pressure variables do not pertain to the nodal (or integration) points, they are not mapped as are the displacement variables.

Let ${}^t \tilde{p}_N(r_N^n, s_N^n)$ be the pressure at the Gauss (integration) point n within an element in the new finite element model

$${}^t \tilde{p}_N(r_N^n, s_N^n) = \sum_{m=1}^{M_N} g_m(r_N^n, s_N^n) {}^t p_N^m, \quad (66)$$

where the variables are defined similarly as for Eq. (65).

Let ${}^t \bar{p}_N^n$ be the pressure obtained by the inverse isoparametric mapping technique at Gauss point n in the new finite element model (evaluated from the old finite element model solution at the (r_O^n, s_O^n) location of element E_O) and N_N be the total number of Gauss points in the element. The number of pressure coefficients is less than the total number of Gauss points in each element. Hence, a least-squares method is used to solve for the unknown pressure coefficients in each element of the new finite element model. The least-squares method is described by minimizing the error

$$E = \sum_{n=1}^{N_N} ({}^t \tilde{p}_N(r_N^n, s_N^n) - {}^t \bar{p}_N^n)^2, \quad (67)$$

with respect to each pressure coefficient. Namely,

$$\frac{\partial E}{\partial {}^t p_N^m} = 0, \quad m = 1, \dots, M_N. \quad (68)$$

This results in M_N simultaneous equations for ${}^t p_N^m$ ($m = 1, \dots, M_N$), and can be written in matrix form as

$$[A] \{P\} = \{G\}, \quad (69)$$

with

$$P_m = {}^t p_N^m, \quad (70)$$

$$A_{lm} = \sum_{n=1}^{N_N} g_l(r_N^n, s_N^n) g_m(r_N^n, s_N^n), \quad (71)$$

$$G_m = \sum_{n=1}^{N_N} g_m(r_N^n, s_N^n) {}^t \bar{p}_N^n, \quad (72)$$

$l = 1, \dots, M_N$ and $m = 1, \dots, M_N$.

We note that the coefficient matrix $[A]$ is symmetric with constant entries since the locations of the Gauss (integration) points in the rs plane are fixed and predetermined if throughout the new mesh the same order of element and numerical integration are used.

4.3. Mapping of contact conditions

For the contact algorithm used here [34], there are three possible contact conditions for the contactor nodes and the contactor segments: not in contact, sliding, and sticking. The conditions of

the contactor nodes in the new finite element model are needed for setting up the contact equations at the start of the next iteration step: two equations are needed for each contactor node that is “sticking”, one for “sliding”, and none for “not in contact”. The conditions of the contactor segments in the new finite element model are needed when calculating the tractions and resultant forces during the iteration. These conditions are derived from the conditions of the contactor nodes and segments in the old finite element model by interpolation, giving preference to “sticking” followed by “sliding” conditions.

4.4. Mapping of history-dependent variables

In elastoplastic analysis using the u/p formulation, the solution variables needed by the new finite element model at time t consist of the displacements ${}^t\mathbf{u}_N$ at each nodal point, the pressure coefficients ${}^t\mathbf{p}_N$ within each element and a list of history-dependent variables ${}^t\mathbf{I}_N$ at each Gauss point. The variables ${}^t\mathbf{u}_N$ and ${}^t\mathbf{p}_N$ are evaluated from ${}^t\mathbf{u}_O$ and ${}^t\mathbf{p}_O$ using the procedures described in Sections 4.1 and 4.2, respectively. In this section, we discuss the evaluation of ${}^t\mathbf{I}_N$.

In elastoplastic analysis we have at each Gauss point of the new finite element model the history-dependent variables,

$${}^t\mathbf{I}_N = \{ {}^t\boldsymbol{\tau}_N, {}^t_0\mathbf{X}_N^p, {}^t\mathbf{e}_N^p, {}^t\mathbf{s}_N, {}^t\chi_N \}, \tag{73}$$

where ${}^t\boldsymbol{\tau}_N$ is the Cauchy stress tensor, ${}^t_0\mathbf{X}_N^p$ is the plastic deformation gradient tensor, ${}^t\mathbf{e}_N^p$ is the equivalent plastic strain, ${}^t\mathbf{s}_N$ is the yield stress and ${}^t\chi_N$ is the elastoplastic flag.

One approach to derive ${}^t\mathbf{I}_N$ would be to use all variables in ${}^t\mathbf{I}_O$ of the old finite element model:

$${}^t\mathbf{I}_O = \{ {}^t\boldsymbol{\tau}_O, {}^t_0\mathbf{X}_O^p, {}^t\mathbf{e}_O^p, {}^t\mathbf{s}_O, {}^t\chi_O \}. \tag{74}$$

Since ${}^t\mathbf{I}_O$ and ${}^t\mathbf{I}_N$ are Gauss point quantities, we would first obtain the smoothed nodal point values for each of the variables in the list ${}^t\mathbf{I}_O$, then use the inverse isoparametric mapping technique of Section 4.1 to transfer these variables to the nodal points of the new finite element model and finally by interpolation obtain the corresponding list of variables at the Gauss points in the new finite element model. This approach, however, is inaccurate and inefficient because of the large number of variables that have to be transferred, and more importantly, may result in a set of values ${}^t\mathbf{I}_N$ that are not self-consistent. For example, the effective stress ${}^t\sigma_N$ may be greater than the yield stress ${}^t\mathbf{s}_N$.

Upon reviewing the elastoplastic formulation, we recognize that the solution variables are inter-related and that for an isotropic hardening elastoplastic material, the list of variables ${}^t\mathbf{I}_N$ at each Gauss point can be derived from the trial elastic deformation gradient at time t (\mathbf{X}_N^e), the equivalent plastic strain at time $t - \Delta t$ (${}^{t-\Delta t}\mathbf{e}_N^p$), the displacements at time t (${}^t\mathbf{u}_N$) and the pressure coefficients at time t (${}^t\mathbf{p}_N$) by the time-integration algorithm. Such a procedure ensures that the consistency requirement is satisfied.

We therefore need to, firstly, transfer only the following list of additional variables from the old finite element model:

$${}^t\tilde{\mathbf{I}}_O = \{ \mathbf{X}_O^e, {}^{t-\Delta t}\mathbf{e}_O^p \}. \tag{75}$$

Note that for a two-dimensional problem in the x - y plane,

$$\mathbf{X}_*^e(1, 3) = \mathbf{X}_*^e(3, 1) = \mathbf{X}_*^e(2, 3) = \mathbf{X}_*^e(3, 2) = 0. \tag{76}$$

Therefore, only six scalar quantities in (75) need to be transferred from the old to the new finite element model.

The mapping of the equivalent plastic strain ${}^{t-\Delta t}e_O^p$ is carried out using the following procedure.

1. Project ${}^{t-\Delta t}e_O^p$ bilinearly to the nodal points in the old finite element model.
2. Obtain the smoothed nodal point equivalent plastic strain $({}^{t-\Delta t}e_O^p)^k$ by taking averages at each nodal point k in the old finite element model.
3. Obtain the physical coordinates $({}^{t-\Delta t}x_N^n, {}^{t-\Delta t}y_N^n)$ for each of the Gauss points (n) in the new finite element model.
4. Identify the old finite element E_O that contains $({}^{t-\Delta t}x_N^n, {}^{t-\Delta t}y_N^n)$ using the procedure of Section 4.1.
5. Obtain the isoparametric coordinates (r_O^n, s_O^n) corresponding to $({}^{t-\Delta t}x_N^n, {}^{t-\Delta t}y_N^n)$ by using the inverse isoparametric mapping technique.
6. The equivalent plastic strain $({}^{t-\Delta t}e_N^p)^n$ at the Gauss point n in the new finite element model is then given by

$$({}^{t-\Delta t}e_N^p)^n = \sum_{k=1}^{K_O} h_k(r_O^n, s_O^n)({}^{t-\Delta t}e_O^p)^k. \quad (77)$$

The same procedure is used for mapping the other variables of ${}^t\tilde{I}_O$ to obtain

$${}^t\tilde{I}_N = \{X_{N,N}^e, {}^{t-\Delta t}e_N^p\}. \quad (78)$$

The yield stress ${}^{t-\Delta t}\sigma_N$ is obtained from the mapped equivalent plastic strain and the strain hardening function (34)

$${}^{t-\Delta t}\sigma_N = Y({}^{t-\Delta t}e_N^p). \quad (79)$$

Now, secondly, with $X_{N,N}^e$, ${}^{t-\Delta t}e_N^p$, ${}^{t-\Delta t}\sigma_N$, ${}^t\mathbf{u}_N$ and ${}^t\mathbf{p}_N$ known, we may proceed to use the time integration algorithm to derive tI_N . The procedure used is described as follows.

1. Obtain the deformation gradient t_0X_N and its determinant.

The deformed configuration of the old finite element model ${}^t\mathbf{x}_O$ is known and the deformed configuration of the new finite element model ${}^t\mathbf{x}_N$ is assumed to occupy the same physical space. Based on this assumption, we have already recovered the deformed configuration of the new finite element model ${}^t\mathbf{x}_N$ and the displacement ${}^t\mathbf{u}_N$ at time t . The reference configuration of the new finite element model ${}^0\mathbf{x}_N$ is obtained from

$${}^0\mathbf{x}_N = {}^t\mathbf{x}_N - {}^t\mathbf{u}_N. \quad (80)$$

The deformation gradient and its determinant are then given by

$${}^t_0X_N = \frac{\partial {}^t\mathbf{x}_N}{\partial {}^0\mathbf{x}_N}, \quad (81)$$

$${}^tJ_N = \det {}^t_0X_N. \quad (82)$$

2. Obtain the plastic deformation gradient ${}^{t-\Delta t}_0 \mathbf{X}_N^p$ at time $t - \Delta t$ and enforce the plastic incompressibility condition:

$${}^{t-\Delta t}_0 \bar{\mathbf{X}}_N^p = (\mathbf{X}_{*N}^e)^{-1} {}^t_0 \mathbf{X}_N, \quad (83)$$

$$\alpha = \det {}^{t-\Delta t}_0 \bar{\mathbf{X}}_N^p, \quad (84)$$

$${}^{t-\Delta t}_0 \mathbf{X}_N^p = \frac{1}{\sqrt[3]{\alpha}} {}^{t-\Delta t}_0 \bar{\mathbf{X}}_N^p. \quad (85)$$

3. Obtain the trial elastic rotation tensor \mathbf{R}_{*N}^e and the trial elastic right stretch tensor \mathbf{U}_{*N}^e by polar decomposition:

$$\mathbf{X}_{*N}^e = \mathbf{R}_{*N}^e \mathbf{U}_{*N}^e. \quad (86)$$

4. Obtain the trial Hencky elastic strain tensor $\boldsymbol{\varepsilon}_{*N}^e$:

$$\boldsymbol{\varepsilon}_{*N}^e = \ln \mathbf{U}_{*N}^e. \quad (87)$$

5. Obtain the deviatoric part of the trial rotated stress tensor $\bar{\boldsymbol{\tau}}_{*N}$:

$$\bar{\boldsymbol{\tau}}'_{*N} = 2\mu \boldsymbol{\varepsilon}'_{*N}. \quad (88)$$

6. Obtain the trial effective stress σ_* :

$$\sigma_* = ({}^t J_N)^{-1} \sqrt{\frac{3}{2} \bar{\boldsymbol{\tau}}'_{*N} \cdot \bar{\boldsymbol{\tau}}'_{*N}}. \quad (89)$$

7. If $\sigma_* < {}^{t-\Delta t} s_N$ then

- (a) process is elastic; set elastoplastic flag to 0

$${}^t \chi_N = 0, \quad (90)$$

- (b) plastic deformation gradient ${}^t_0 \mathbf{X}_N^p$, equivalent plastic strain ${}^t e_N^p$, and yield stress ${}^t s_N$ are not changed:

$${}^t_0 \mathbf{X}_N^p = {}^{t-\Delta t}_0 \mathbf{X}_N^p, \quad (91)$$

$${}^t e_N^p = {}^{t-\Delta t} e_N^p, \quad (92)$$

$${}^t s_N = {}^{t-\Delta t} s_N, \quad (93)$$

- (c) the trial stress is the actual stress:

$${}^t_0 \bar{\boldsymbol{\tau}}_N = \bar{\boldsymbol{\tau}}'_{*N} - {}^t \tilde{p}_N \mathbf{1}, \quad (94)$$

where ${}^t \tilde{p}_N$ is the mixed-interpolated pressure at the integration point which has already been obtained from mapping using the procedure of Section 4.2; the Cauchy stress tensor ${}^t \boldsymbol{\tau}_N$ is then given by

$${}^t \boldsymbol{\tau}_N = ({}^t J_N)^{-1} \mathbf{R}_{*N}^e {}^t_0 \bar{\boldsymbol{\tau}}_N (\mathbf{R}_{*N}^e)^T, \quad (95)$$

- (d) exit time-integration algorithm.

8. If $\sigma_* \geq {}^{t-\Delta t} s_N$ then:

(a) process is elastoplastic; set elasto-plastic flag to 1

$${}^t \chi_N = 1, \quad (96)$$

(b) continue.

9. Obtain ${}^t e_N^p$ by solving

$$3\mu({}^t e_N^p - {}^{t-\Delta t} e_N^p) + {}^t J_N [Y({}^t e_N^p) - \sigma_*] = 0. \quad (97)$$

10. Obtain yield stress ${}^t s_N$ from

$${}^t s_N = Y({}^t e_N^p). \quad (98)$$

11. Obtain $\Delta\lambda$ from

$$\Delta\lambda = \frac{3({}^t e_N^p - {}^{t-\Delta t} e_N^p)}{2({}^t J_N {}^t s_N)}. \quad (99)$$

12. Obtain the Cauchy stress ${}^t \tau_N$ using

$${}^t_0 \bar{\tau}'_N = \frac{\bar{\tau}'_N}{1 + 2\mu \Delta\lambda}, \quad (100)$$

$${}^t_0 \bar{\tau}_N = {}^t_0 \bar{\tau}'_N - {}^t \tilde{p}_N \mathbf{1}, \quad (101)$$

$${}^t \tau_N = ({}^t J_N)^{-1} \mathbf{R}^{\varepsilon_N} {}^t_0 \bar{\tau}_N (\mathbf{R}^{\varepsilon_N})^T. \quad (102)$$

13. Obtain the plastic deformation gradient ${}^t_0 X_N^p$ from

$${}^t_0 X_N^p = \exp(\Delta\lambda {}^t_0 \bar{\tau}'_N) {}^{t-\Delta t} X_N^p. \quad (103)$$

5. Numerical examples

In this section we present the solution of some elastic and elastoplastic problems with large displacement, large strain and contact conditions to demonstrate the use of the proposed adaptive procedures.

The EIS indicator is employed for assessing the accuracy of the solution at every time step (and in the examples below the values of the EIS are referred to as the “error in stress”). When this error indicator exceeds an acceptable level, the macro-element mesh generator is used to create a more suitable mesh in the deformed configuration. The mapping procedures for displacement, pressure, contact variables and history-dependent variables are then employed to transfer the solution variables from the old mesh to the new mesh, and the analysis is continued from the current time step until the error as estimated by the EIS indicator again becomes unacceptably large. In analyses involving elastoplastic response, the EPSI indicator is used to estimate the error in the plastic strain increments created by nonradial loading conditions. This indicator is used to control adaptively the size of the incremental load-steps during the analysis so that accurate plastic strain increments are obtained throughout the response prediction.

5.1. Surface wrinkling of rubber seal

We consider a rubber seal that undergoes large deformations. Fig. 13 shows the seal in its initial configuration, mounted between an outer stationary cylinder and an inner moving cylinder. The objective is to obtain accurate force and stress predictions as the inner cylinder moves downward by 43 mm in 43 equal steps. The rubber material is modeled as a Mooney–Rivlin material, with material constants $C_1 = 0.293$ MPa, $C_2 = 0.177$ MPa, and $\kappa = 1410$ MPa.

With a coarse mesh, Mesh 1 (as shown in Fig. 14), we succeed in pulling the inner cylinder downward from start to finish without any difficulty because no wrinkle occurs. The stresses predicted by this model, however, are not accurate. Errors in pressure and effective stress, as given by the EIS indicators, are both greater than 10% right from the beginning.

For better stress predictions, we proceed to solve this problem adaptively. Mesh 2 (shown in Fig. 15) is an adaptively refined model that predicts the pressure and effective stress to within an accuracy of 5% everywhere, except near the four sharp corners (A, B, C and D in Fig. 15). With Mesh 2, accurate stresses are obtained until a deflection of 32 mm. Beyond this deflection, the error in effective stress exceeds 5% next to point A and continues to spread out and increase. At a deflection of 35 mm, the error is above 10% at point G and, also, the tangential principal stress at point G becomes highly compressive, indicating that a wrinkle may soon initiate near this location.

We therefore remesh the region A-B-E-F at a deflection of 31 mm, and remodel the contact surfaces by introducing a target surface to the right of point G in anticipation of the contact by the contactor surface to the left of point G. This mesh, Mesh 3, is shown in Fig. 16.

At a deflection of 36 mm, the rubber seal starts to wrinkle about point G as shown in Fig. 17. With Mesh 3, we succeed in pulling the rubber seal to the final deflection of 43 mm. The final shape of the rubber seal is shown in Fig. 18 and the pressure distribution in the seal in this position is shown in Fig. 19. The error indicator on the pressure gives values slightly above 10% after wrinkling occurred.

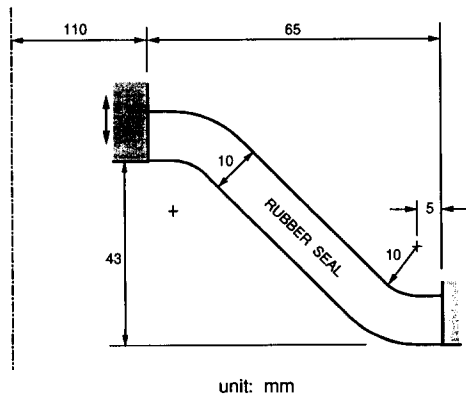


Fig. 13. Rubber seal – Surface wrinkling problem.

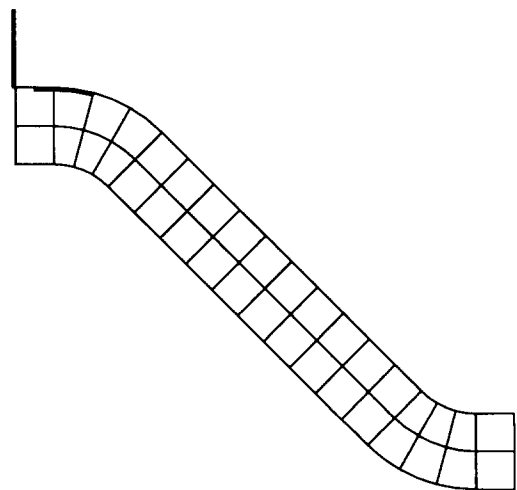


Fig. 14. Mesh 1 for the surface wrinkling problem.

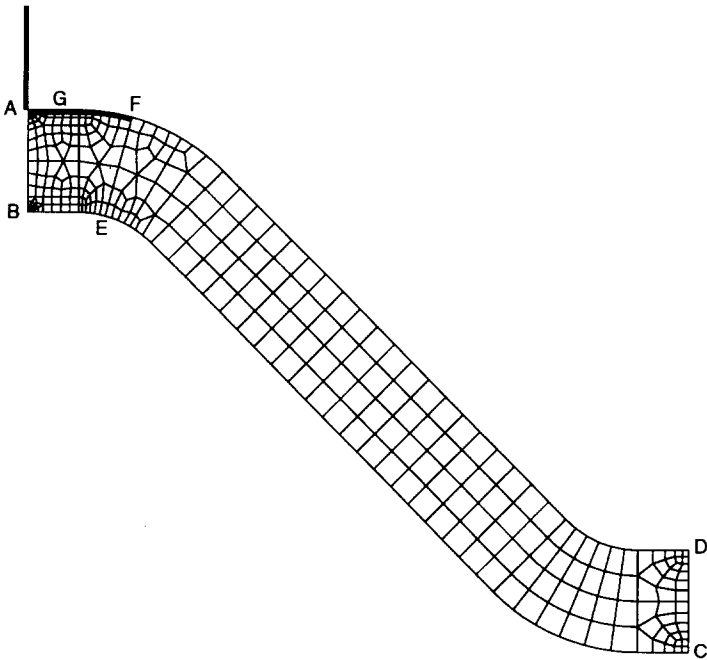


Fig. 15. Mesh 2 for the surface wrinkling problem.

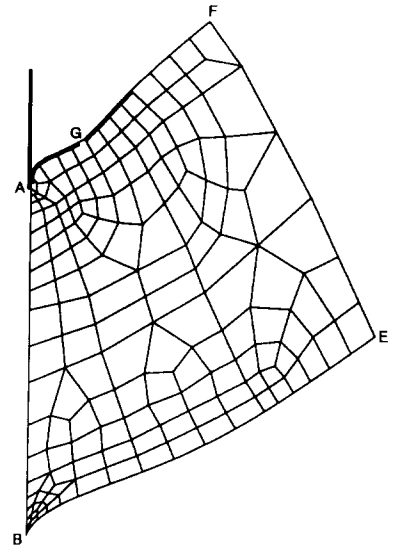


Fig. 16. Mesh 3 for the surface wrinkling problem at deflection of 31 mm.

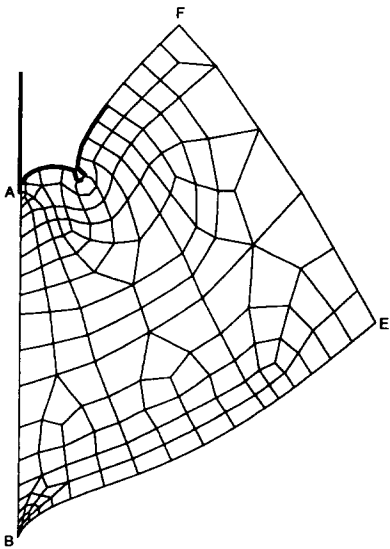


Fig. 17. Mesh 3 at deflection of 36 mm.

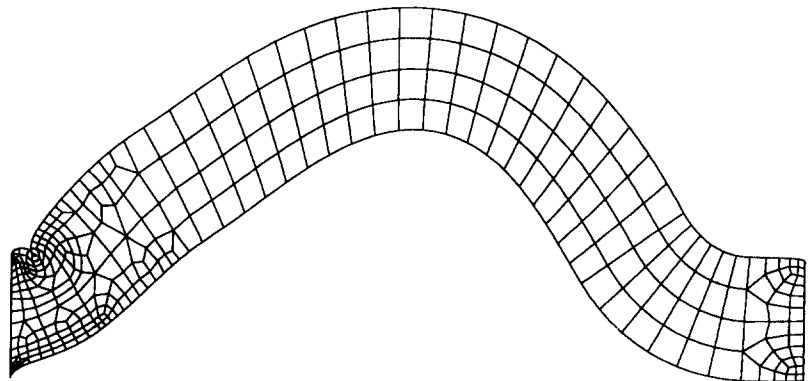


Fig. 18. Final shape of rubber seal obtained with Mesh 3.

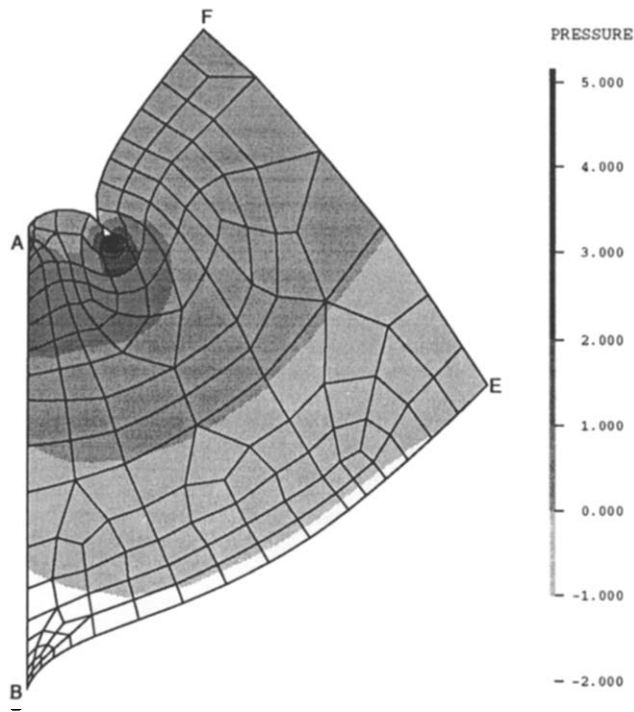


Fig. 19. Pressure distribution in rubber seal in final position obtained with Mesh 3.

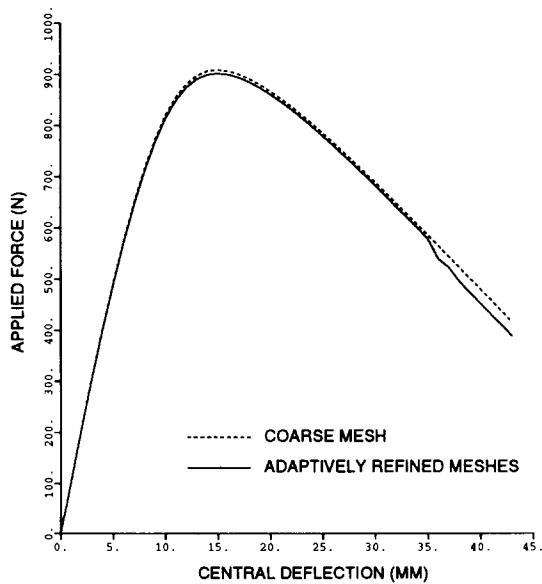


Fig. 20. Force vs. deflection curves for the rubber seal.

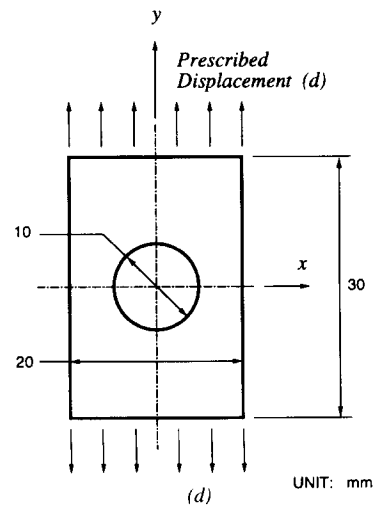


Fig. 21. Thick specimen with a central hole.

The force vs. deflection curve obtained adaptively (using Meshes 2 and 3) is shown in Fig. 20. The curve obtained with the coarse mesh (Mesh 1) compares very well with that obtained with the adaptive meshes, although of course the coarse mesh could not predict the wrinkle nor the pressure distribution around the wrinkle.

5.2. Localized deformation in a thick specimen

We consider the use of our adaptive scheme to study a problem with a shear band formation that causes localized large deformations. The problem is described in Fig. 21. The specimen is modeled as an elastic perfectly-plastic solid in plane strain conditions with Young's modulus $E = 100$ GPa, Poisson's ratio $\nu = 0.3$ and yield stress $s = 100$ MPa.

Due to symmetry conditions, only one quarter of the specimen needs be considered. We start with the initial model (Mesh 1) shown in Fig. 22 and apply the displacement ($d = 0$ to 1.5 mm) along line A–A' in the figure. An initial incremental load step size of $\Delta d = 0.01$ mm is used. At time-step 2 ($d = 0.02$), both the error in the effective stress (as estimated by our EIS indicator) and the error in the plastic strain increment (as estimated by our EPSI indicator) have exceeded 10% as

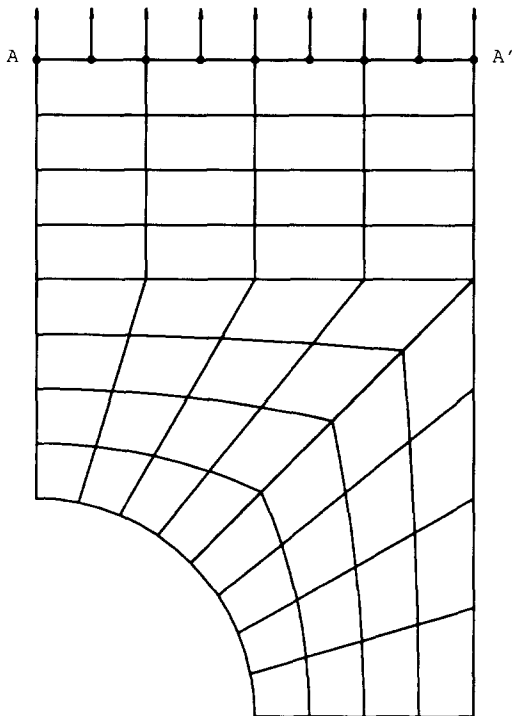


Fig. 22. Mesh 1 for the plane strain problem.

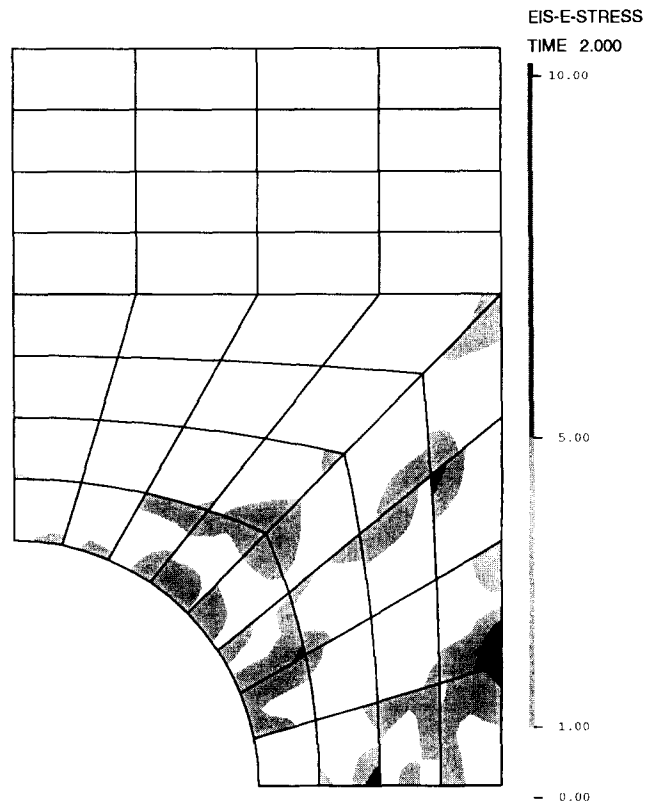


Fig. 23. Percentage error in effective stress at $d = 0.02$ using Mesh 1.

shown in Figs. 23 and 24, respectively. A refined finite element model together with smaller sizes of incremental loads should therefore be used.

The refined model (Mesh 2) is shown in Fig. 25. We have focused the refinements in the region where the value of the EIS indicator is high as well as in the region where there is a significant amount of error in the plastic strain increment, and we also decrease the size of the incremental loads by a factor of two to $\Delta d = 0.005$. With Mesh 2 and the smaller incremental loads, the errors in the effective stress and plastic strain increment are less than 5% from the beginning of the analysis. At time-step 4 ($d = 0.02$) these errors are as shown in Figs. 26 and 27, respectively, for comparison with those obtained using Mesh 1.

The error in the plastic strain increment as given by the EPSI indicator gradually decreases as deformation progresses. We therefore double the size of the incremental loads from time-step 11 onwards. At time-step 20, a shear band becomes noticeable from the deformation pattern. The equivalent plastic strain obtained using Mesh 2 is shown in Fig. 28. This figure shows the localized nature of the shear band. (For comparison, we also show the corresponding results obtained using Mesh 1 in Fig. 29).

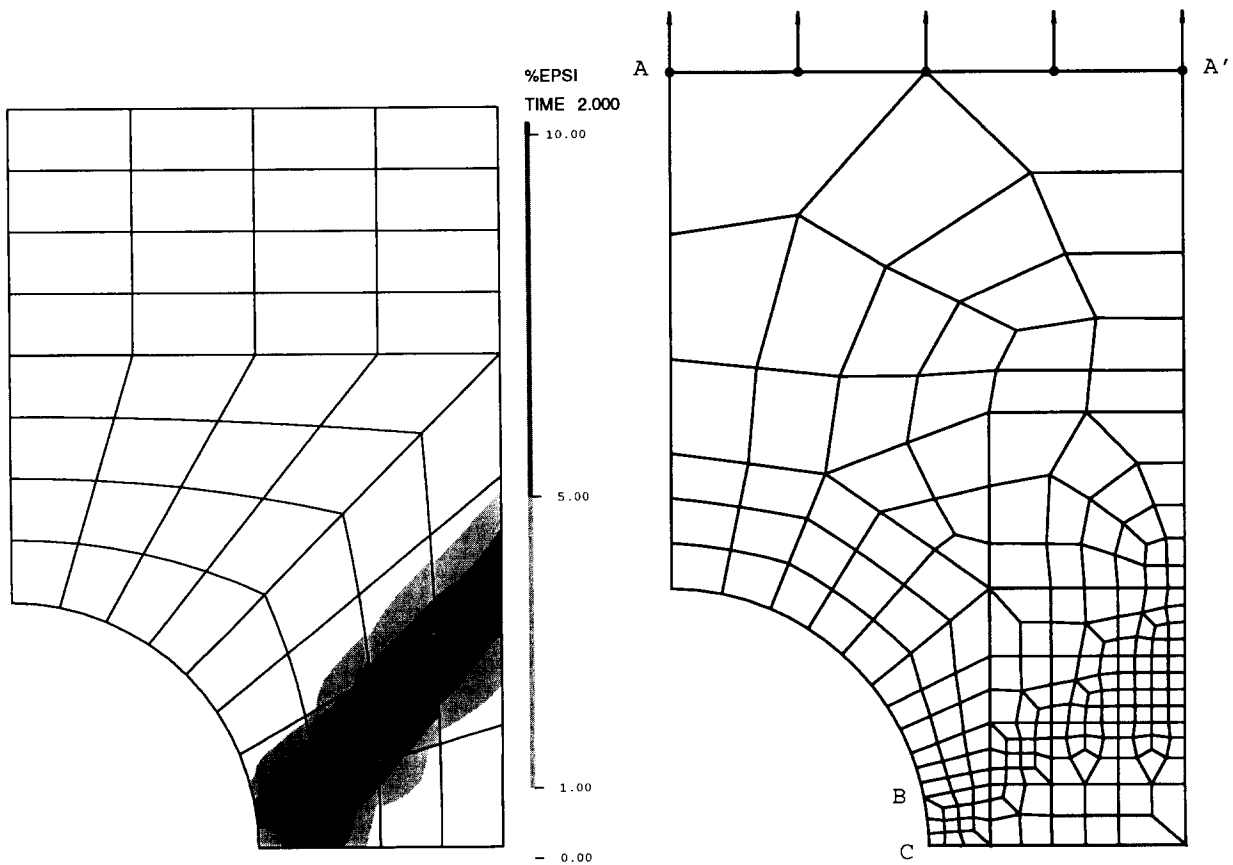


Fig. 24. Percentage error in plastic strain increment at $d = 0.02$ using Mesh 1.

Fig. 25. Mesh 2 for the thick plate problem.

5.3. Analysis of a heading process

The metal forming industries are laden with problems that involve large strain elastoplastic conditions which are not easily solved using the finite element method. With a coarse finite element model, little difficulties are encountered during the analysis; however, the resulting stress predictions are frequently not accurate. With a fine model, the accuracy in stress prediction improves; however, the solution cost is substantially higher and the analysis may not proceed to completion because, for example, the elements next to stress concentration points may become badly distorted.

In this section we present an example of the use of our adaptive procedures to study the problem of a cylindrical workpiece undergoing a heading operation. The problem is described in Fig. 30. The workpiece is a typical ductile material with Young’s modulus $E = 70 \text{ GPa}$, Poisson’s ratio $\nu = 0.33$, yield stress $s = 70 \text{ MPa}$ and strain hardening modulus $E_T = 300 \text{ MPa}$. It is rigidly clamped onto the grip die during the heading operation. The heading tool and the grip die are rather stiff (in comparison with the workpiece) and are therefore modeled as rigid surfaces in the finite element model. Friction between the workpiece and the tools is negligible. Our objective is to

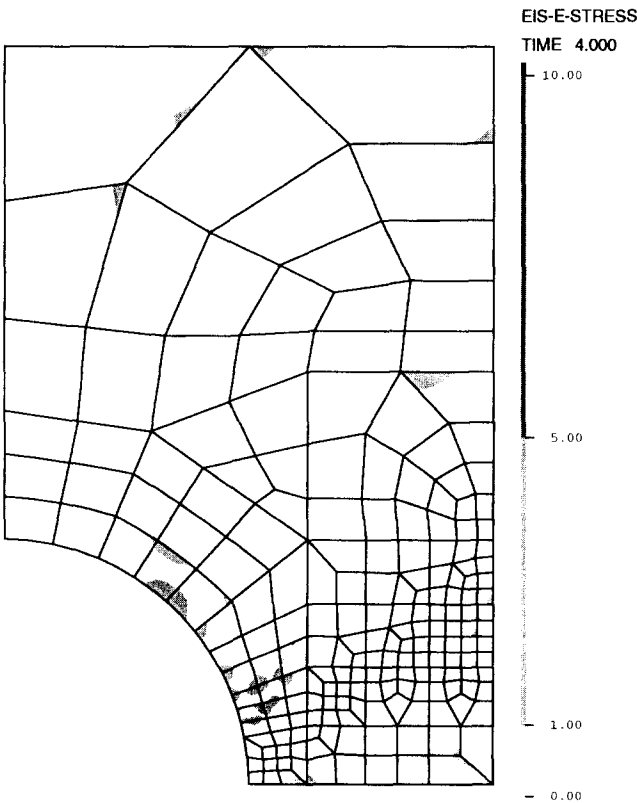


Fig. 26. Percentage error in effective stress at $d = 0.02$ using Mesh 2.

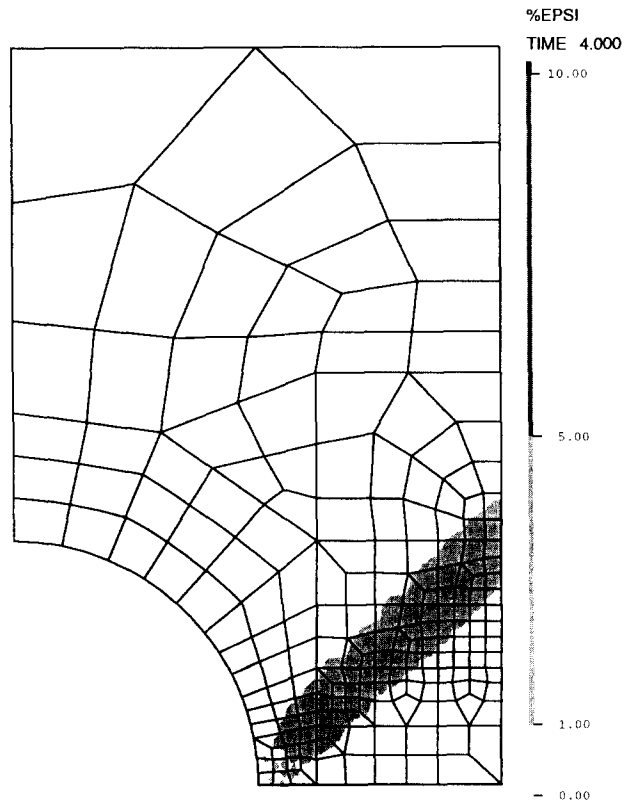


Fig. 27. Percentage error in plastic strain increment at $d = 0.02$ using Mesh 2.

predict accurately the stresses and deformations of the workpiece as the heading tool travels downwards by 5.6 mm.

We begin with a typical coarse mesh shown in Fig. 31 and an incremental load step size of 0.001 mm. At time-step 2, the errors in the effective stress and pressure (as estimated by our EIS indicators) have exceeded 10% as shown in Figs. 32 and 33, respectively. A refined model (Mesh 2 as shown in Fig. 34) is therefore created based on the distribution of error estimated by the EIS indicators and an accuracy level of 5%. The error in the plastic strain increment for Mesh 1 (estimated by our %EPSI indicator) is only 1.6% at time-step 2. We therefore also double the load step size for the analysis using Mesh 2. The actual load used at each time-step for the complete analysis is shown in Fig. 35. The sizes of the incremental loads were chosen to maintain the EPSI indicator at less than 10%. An automatic-time-stepping (ATS) scheme is also used by the contact algorithm to further subdivide the load steps whenever the analysis encounters difficulties in establishing the equilibrium conditions [22].

With Mesh 2, the errors in the effective stress and pressure are less than 5% except for the six elements next to the singularity at corner A. We therefore accept Mesh 2 as a suitable mesh to start the analysis. Throughout the solution, the error in pressure is less than that of the error in effective

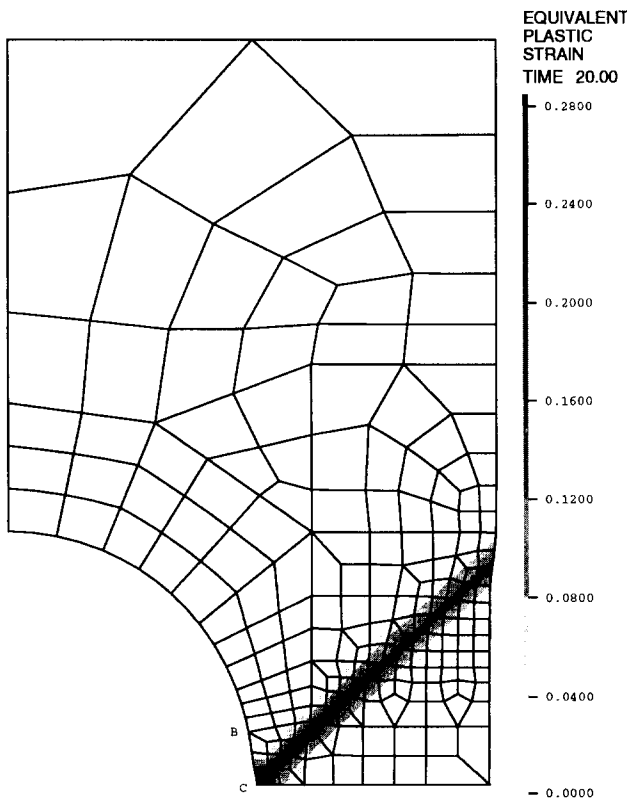


Fig. 28. Equivalent plastic strain at $d = 0.15$ predicted using Mesh 2.

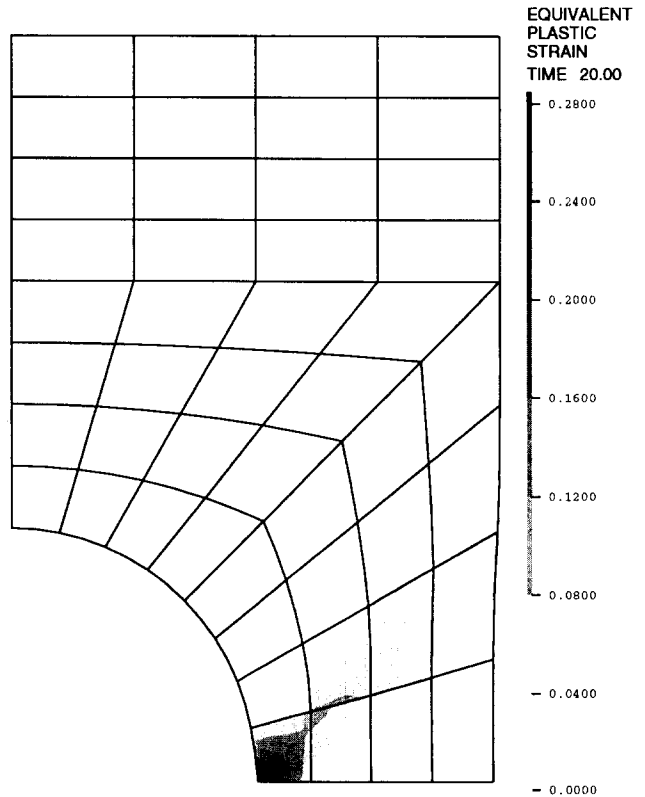


Fig. 29. Equivalent plastic strain at $d = 0.15$ predicted using Mesh 1.

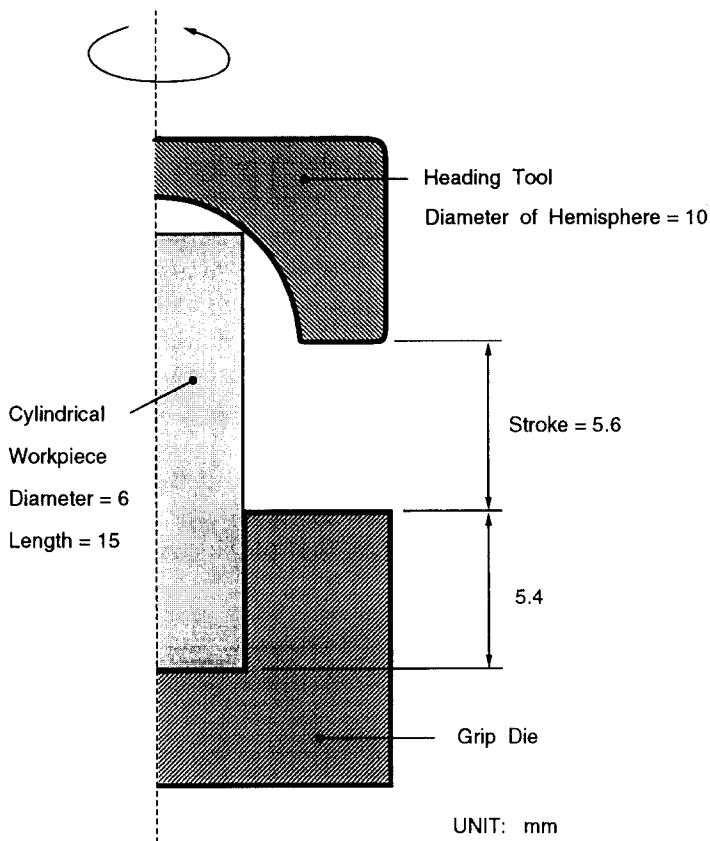


Fig. 30. Problem of a cylindrical workpiece undergoing a heading process.

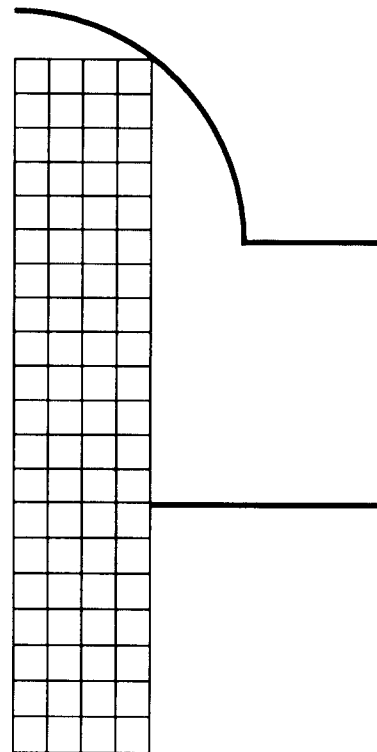


Fig. 31. Mesh 1 for the heading problem.

stress. At time-step 51, the error in the effective stress has just exceeded 10% at point C and at time-step 55, this error has also exceeded 10% at points B and D as shown in Fig. 36. We therefore refine the model around points B, C and D at time-step 50. With this refined model (Mesh 3), the error in the effective stress at time-step 55 is as shown in Fig. 37; the maximum error has been reduced to about 5%.

As the analysis continues, errors in the effective stress and pressure are within 10% everywhere except for the elements around points A and B where very high stress concentrations are present. Since very small elements are already used in these locations, no further refinement is performed. Element distortions become the critical factor beyond time-step 90. A very high pressure gradient around point B causes elements in this region to quickly become too distorted for the analysis to proceed. We have to remesh at time-steps 90, 104, 116 and 122 using Meshes 4 to 7 (not shown) to remove excessive distortions so that the analysis can proceed to completion at time-step 135.

The final deformed shape and pressure distribution within the workpiece obtained with Mesh 7 are shown in Fig. 38. The corresponding results obtained with Mesh 1 are shown in Fig. 39. (With Mesh 1, there was no difficulty in reaching the final configuration in 100 time-steps.) The

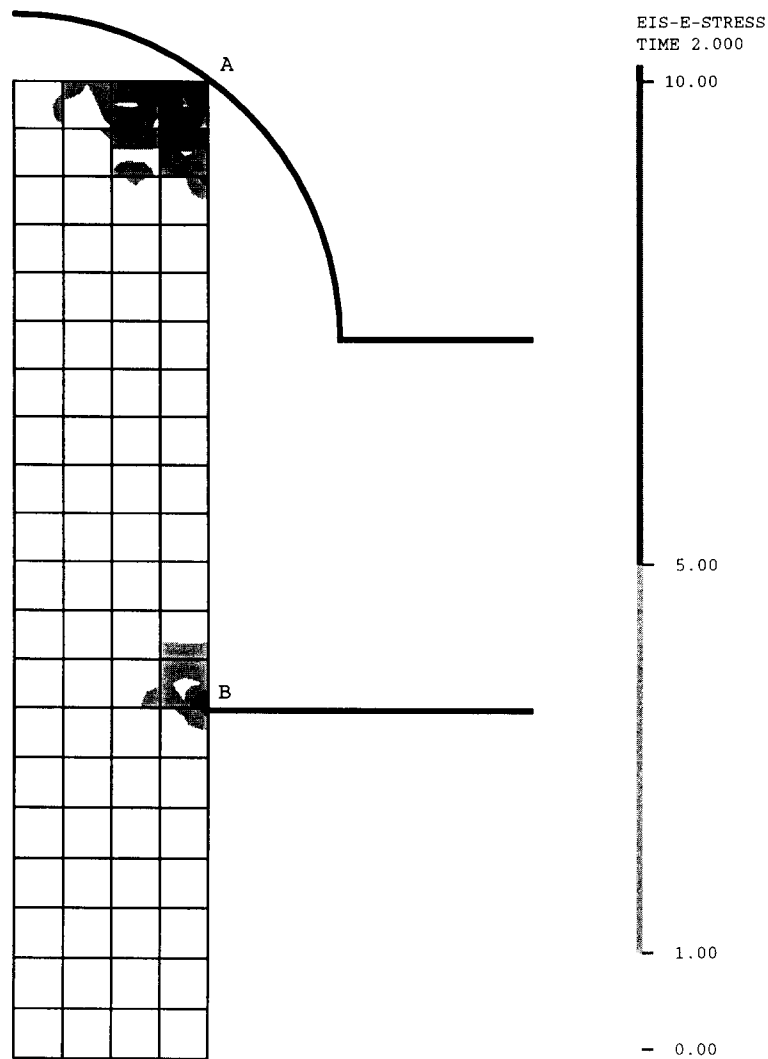


Fig. 32. Percentage error in effective stress at time-step 2 using Mesh 1.

force vs. deflection curves are shown in Fig. 40. With the coarse mesh (Mesh 1), the load–deflection curve obtained is almost the same as that obtained with the adaptive meshes – except the final load reached is lower. However, the pressure distribution and pressure gradient around point B are quite different from those predicted with the adaptive meshes.

6. Conclusions

In this work we formulated and developed a system of adaptive procedures that can be used for the finite element analysis of nonlinear elastic and elastoplastic problems to ensure that the stresses are accurately predicted.

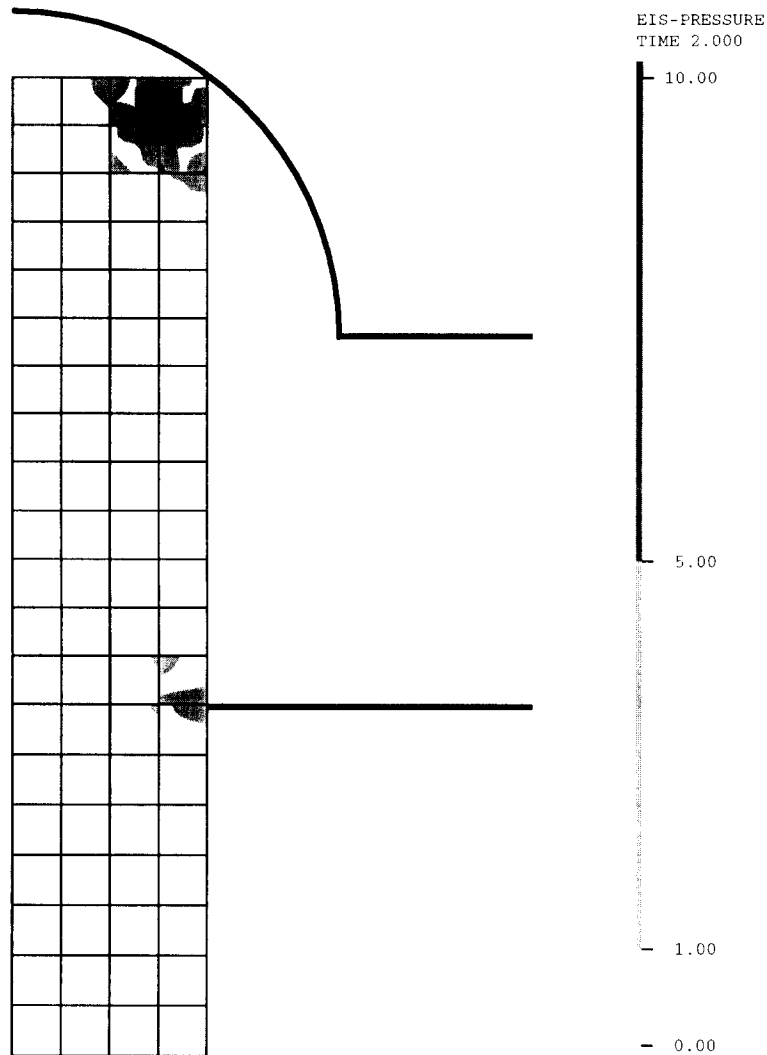


Fig. 33. Percentage error in pressure at time-step 2 using Mesh 1.

The developed procedures include a pointwise indicator for the error in stresses, a pointwise indicator for the error in plastic strain increments, a quadrilateral element mesh generator for generating completely new meshes on the deformed configuration of the body, and several mapping procedures for transferring state variables and history-dependent variables accurately across models. These procedures constitute the ingredients of a proposed adaptive scheme that was demonstrated to be effective in the solution of some typical nonlinear engineering problems. It is deemed that such scheme would be used in an effective way interactively as the analysis proceeds.

An important observation of this work, also emphasized earlier already [24], is that accurate stress prediction in nonlinear finite element analysis frequently requires the use of error measures.

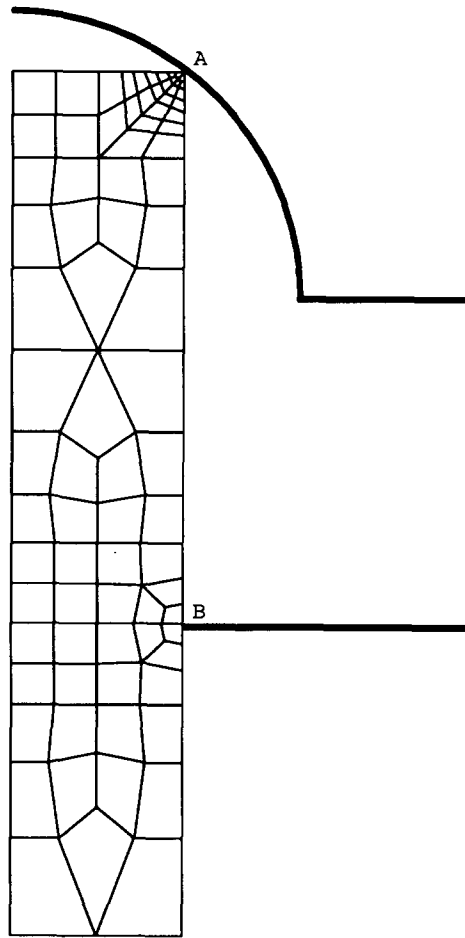


Fig. 34. Mesh 2 for the heading problem.

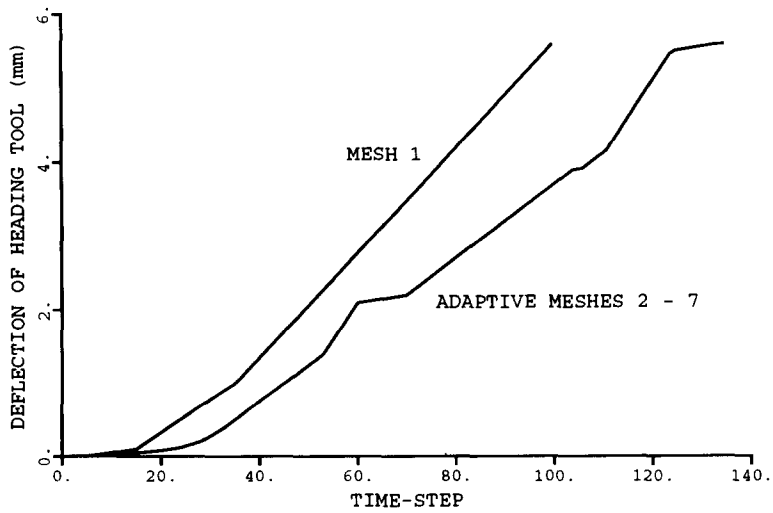


Fig. 35. Adaptively derived deflection loads for the heading problem.

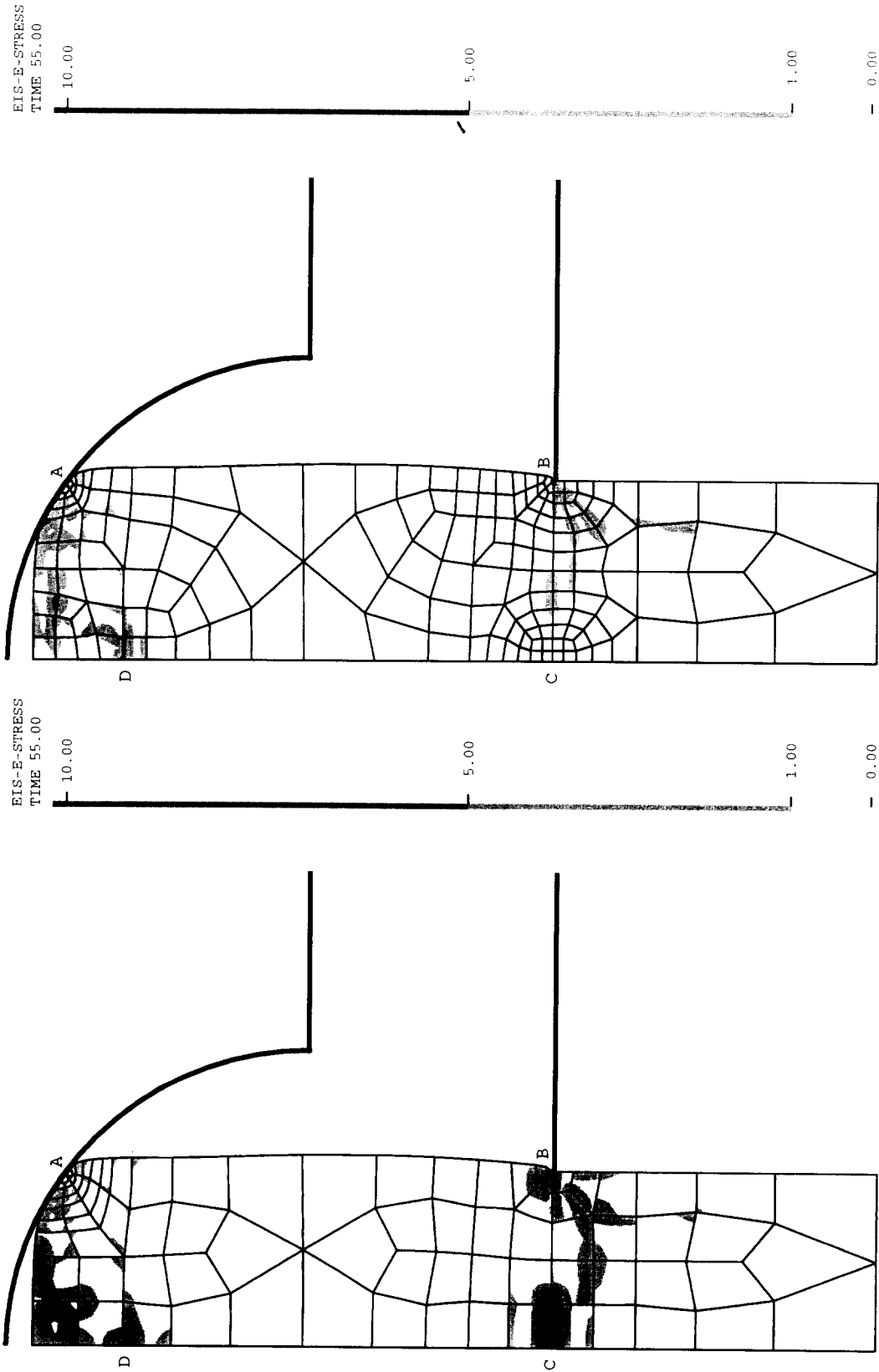


Fig. 36. Percentage error in effective stress at time-step 55 using Mesh 2.

Fig. 37. Percentage error in pressure at time-step 55 using Mesh 3.

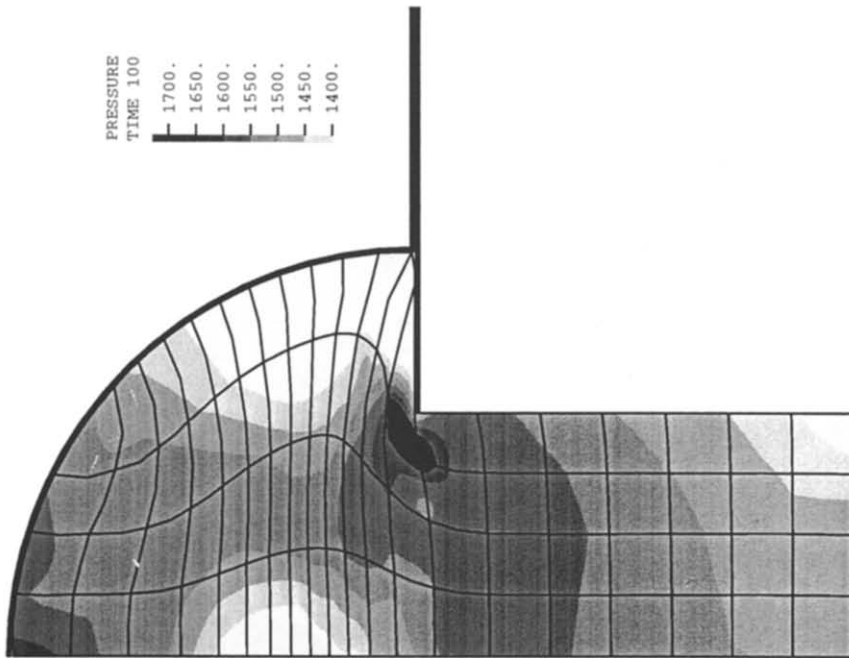


Fig. 39. Pressure distribution in the final position predicted using Mesh 1.

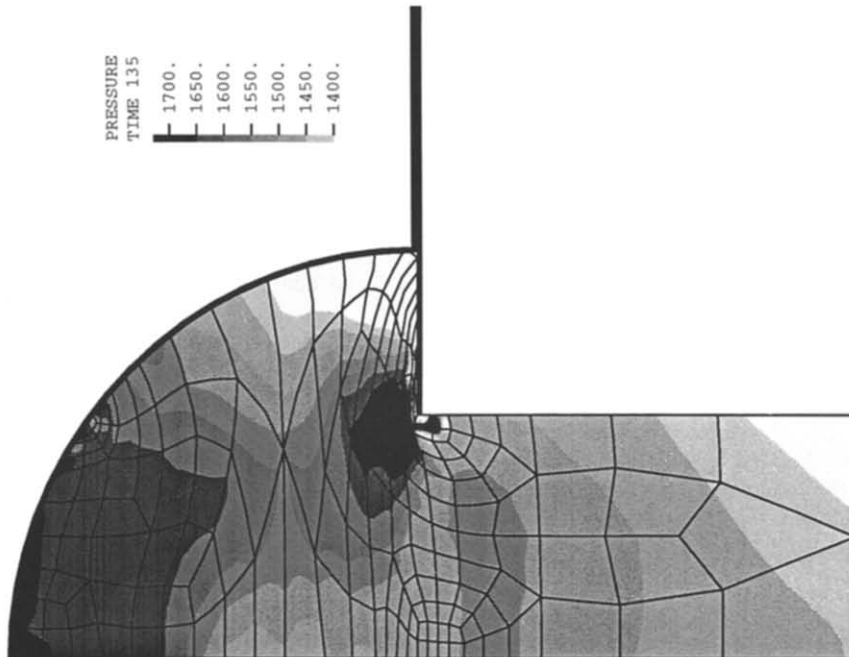


Fig. 38. Pressure distribution in the final position predicted using Mesh 7.

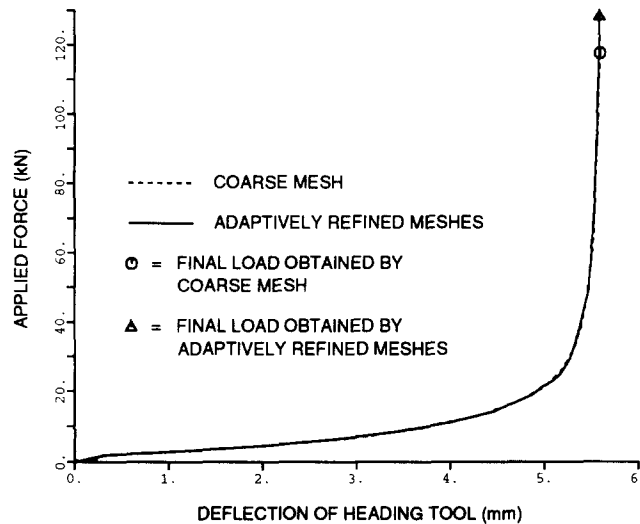


Fig. 40. Force vs. deflection curves for the heading process.

Indeed, a coarse mesh may give a reasonable load- deflection prediction without any difficulties but may totally miss certain physical phenomena (such as wrinkling and shear band formation).

References

- [1] K.J. BATHE, *Finite Element Procedures in Engineering Analysis*, Prentice-Hall, Englewood Cliffs, NJ, 1982.
- [2] I. BABUŠKA and W.C. RHEINBOLDT, "Error estimates for adaptive finite element computations", *SIAM J. Numer. Anal.* **15** (4), pp. 736–754, 1978.
- [3] T. SUSSMAN and K.J. BATHE, "Studies of finite element procedures – stress band plots and the evaluation of finite element meshes", *Eng. Comput.* **3**, pp. 178–191, 1986.
- [4] O.C. ZIENKIEWICZ and J.Z. ZHU, "A simple error estimator and adaptive procedure for practical engineering analysis", *Int. J. Numer. Methods Eng.* **24**, pp. 337–357, 1987.
- [5] J.T. ODEN, L. DEMKOWICZ, W. RACHOWICZ and T.A. WESTERMANN, "Toward a universal $h-p$ adaptive finite element strategy. Part 2. A posteriori error estimation", *Comput. Methods Appl. Mech. Eng.* **77**, pp. 113–180, 1989.
- [6] O.C. ZIENKIEWICZ and J.Z. ZHU, "The superconvergent patch recovery and a posteriori error estimates. Part 1. The recovery technique", *Int. J. Numer. Methods Eng.* **33**, pp. 1331–1364, 1992.
- [7] K.J. BATHE and S.W. CHAE, "On discretization in adaptive finite element analysis", in: C. Chryssostomidis (ed.), *Automation in the Design and Manufacture of Large Marine Systems*, Hemisphere Publ. Corp., 1990.
- [8] O.C. ZIENKIEWICZ, G.C. HUANG and Y.C. LIU, "Adaptive FEM computation of forming processes – application to porous and non-porous materials", *Int. J. Numer. Methods Eng.* **30**, pp. 1527–1553, 1990.
- [9] K. KATO, N.S. LEE and K.J. BATHE, "Adaptive finite element analysis of large strain elastic response", *Comput. Struct.* **47** (4/5) pp. 829–855, 1993.
- [10] I. BABUŠKA, B.A. SZABÓ and I.N. KATZ. "The p -version of the finite element method", *SIAM. J. Numer. Anal.* **18** (3), pp. 515–545, 1981.
- [11] I. BABUŠKA and B.A. SZABÓ, "On the rates of convergence of the finite element method", *Int. J. Numer. Methods Eng.* **18**, pp. 323–341, 1982.
- [12] B.A. SZABÓ, "Estimation and control of error based on p -convergence", in: I. Babuška, O.C. Zienkiewicz, J. Gago, and E.R. de A. Oliveira (eds.), *Accuracy Estimates and Adaptive Refinements in Finite Element Computations*, Ch. 3, Wiley, New York, pp. 61–77, 1986.

- [13] B. GUO and I. BABUŠKA, “The h - p version of the finite element method: part 1 the basic approximation results”, *Computat. Mech.* **1**, pp. 21–41, 1986.
- [14] L. DEMKOWICZ, J.T. ODEN, W. RACHOWICZ and O. HARDY, “Toward a universal h - p adaptive finite element strategy. part 1. Constrained approximation and data structure”, *Comput. Methods Appl. Mech. Eng.* **77**, pp. 79–112, 1989.
- [15] O.C. ZIENKIEWICZ, J.Z. ZHU and N.G. GONG, “Effective and practical h - p -version adaptive analysis procedures for the finite element method”, *Int. J. Numer. Methods Eng.* **28**, pp. 879–891, 1989.
- [16] M.K. GEORGES and M.S. SHEPHARD, “Automated adaptive two-dimensional system for the hp -version of the finite element method”, *Int. J. Numer. Methods Eng.* **32**, pp. 867–893, 1991.
- [17] K.J. BATHE, N.S. LEE and M.L. BUCALEM, “On the use of hierarchical models in engineering analysis”, *Comput. Methods Appl. Mech. Eng.* **82** (1–3), pp. 5–26, 1990.
- [18] J.H. CHENG and N. KIKUCHI, “A mesh re-zoning technique for finite element simulations of metal forming processes”, *Int. J. Numer. Methods Eng.* **23**, pp. 219–228, 1986.
- [19] J.H. CHENG, “Automatic adaptive remeshing for finite element simulation of forming processes”, *Int. J. Numer. Methods Eng.* **26**, pp. 1–18, 1988.
- [20] P.L. BAEHMANN, M.S. SHEPHARD, R.A. ASHLEY and A. JAY, “Automated metalforming modeling utilizing adaptive remeshing and evolving geometry”, *Comput. Struct.* **30** (1/2), pp. 319–325, 1988.
- [21] H.T.Y. YANG, M. HEINSTEIN and J.-M. SHIH, “Adaptive 2D finite element simulation of metal forming processes”, *Int. J. Numer. Methods Eng.* **28**, pp. 1409–1428, 1989.
- [22] ADINA R&D, “ADINA – A finite element program for automatic dynamic incremental nonlinear analysis”, Reports, ADINA R&D, Watertown, MA.
- [23] N.S. LEE and K.J. BATHE, “Effects of element distortions on the performance of isoparametric elements”, *Int. J. Numer. Methods Eng.* **36**, pp. 3553–3576, 1993.
- [24] T. SUSSMAN and K.J. BATHE, “A finite element formulation for nonlinear incompressible elastic and inelastic analysis”, *Comput. Struct.* **26**, pp. 357–409, 1987.
- [25] D. CHAPELLE and K.J. BATHE, “The inf-sup test”, *Comput. Struct.* **47** (4/5), pp. 537–545, 1993.
- [26] F. BREZZI and K.J. BATHE, “A discourse on the stability conditions for mixed finite element formulations”, *Comput. Methods Appl. Mech. Eng.* **82** (1–3) pp. 27–57, 1990.
- [27] E. HINTON and J.S. CAMPBELL, “Local and global smoothing of discontinuous finite element functions using a least squares method”, *Int. J. Numer. Methods Eng.* **8**, pp. 461–480, 1974.
- [28] A.L. ETEROVIC and K.J. BATHE, “A hyperelastic-based large strain elasto-plastic constitutive formulation with combined isotropic-kinematic hardening using the logarithmic stress and strain measures”, *Int. J. Numer. Methods Eng.* **30**, pp. 1099–1114, 1990.
- [29] S.A. COONS, “Surfaces for computer-aided design of space forms”, Report MAC-TR-44. MIT, Cambridge, MA, 1967.
- [30] W.A. COOK, “Body oriented (natural) co-ordinates for generating three-dimensional meshes”, *Int. J. Numer. Methods Eng.* **8**, pp. 27–43, 1974.
- [31] R. HABER, M.S. SHEPHARD, J.F. ABEL, R.H. GALLAGHER and D.P. GREENBERG, “A general two-dimensional, graphical finite element preprocessor utilizing discrete transfinite mappings”, *Int. J. Numer. Methods Eng.* **17**, pp. 1015–1044, 1981.
- [32] V. MURTI and S. VALLIAPPAN, “Numerical inverse isoparametric mapping in remeshing and nodal quantity contouring”, *Comput. Struct.* **22** (6), pp. 1011–1021, 1986.
- [33] R.H. CRAWFORD, D.C. ANDERSON and W.N. WAGGENSPACK, “Mesh rezoning of 2D isoparametric elements by inversion”, *Int. J. Numer. Methods Eng.* **28**, pp. 523–531, 1989.
- [34] K.J. BATHE and A. CHAUDHARY, “A solution method for planar and axisymmetric contact problems”. *Int. J. Numer. Methods Eng.* **21**, pp. 65–88, 1985.